

Allosteric rescue of catalytically impaired ATP phosphoribosyltransferase variants links protein dynamics to active-site electrostatic preorganisation

Received: 29 May 2022

Accepted: 11 November 2022

Published online: 09 December 2022

 Check for updates

Gemma Fisher¹, Marina Corbella², Magnus S. Alphey¹, John Nicholson¹, Benjamin J. Read¹, Shina C. L. Kamerlin^{2,3}✉ & Rafael G. da Silva¹✉

ATP phosphoribosyltransferase catalyses the first step of histidine biosynthesis and is controlled via a complex allosteric mechanism where the regulatory protein HisZ enhances catalysis by the catalytic protein HisG₅ while mediating allosteric inhibition by histidine. Activation by HisZ was proposed to position HisG₅ Arg56 to stabilise departure of the pyrophosphate leaving group. Here we report active-site mutants of HisG₅ with impaired reaction chemistry which can be allosterically restored by HisZ despite the HisZ:HisG₅ interface lying ~20 Å away from the active site. MD simulations indicate HisZ binding constrains the dynamics of HisG₅ to favour a preorganised active site where both Arg56 and Arg32 are poised to stabilise leaving-group departure in WT-HisG₅. In the Arg56Ala-HisG₅ mutant, HisZ modulates Arg32 dynamics so that it can partially compensate for the absence of Arg56. These results illustrate how remote protein-protein interactions translate into catalytic resilience by restoring damaged electrostatic preorganisation at the active site.

Robust reaction rate enhancement and allosteric regulation are hallmarks of enzyme catalysis, and both aspects may be at least in part underpinned by protein conformational flexibility^{1–3}. The catalytic process of enzymes can be significantly ascribed to substrate binding to an electrostatically preorganised active site, which minimises the reorganisation energy required for optimum stabilisation of the charge redistribution as the reaction progresses from the reactant state to the transition state⁴. Yet several lines of evidence also suggest a contribution from protein dynamics^{5–8}, from nonstatistical, femtosecond-timescale vibrations coupled directly to transition-state barrier crossing^{6,8}, to slower, thermally equilibrated motions reshaping the enzyme conformational ensemble towards populations where active-site preorganisation is optimised⁵. Nonetheless, this topic is still controversial possibly due to the inherent flexibility of proteins which makes it difficult to isolate motions that may have evolved to facilitate reaction^{7,9,10}.

Allosteric modulation of enzymes, i.e. the alteration of reaction rate and/or substrate affinity upon ligand binding to, mutation of, or post-translational modification at a site remote from the active site, is a fundamental regulatory mechanism of biochemical reactions^{11,12}. It finds applications in drug discovery to facilitate drug-target selectivity as allosteric sites tend to be less conserved than active sites across homologous proteins^{13,14}, and in enzyme engineering and synthetic biology, where allosteric control may need to be introduced or, more often, eliminated^{15,16}. While enzymes subject to allosteric regulation by ligand binding can be broadly classified as *K*-type, those where substrate affinity is altered, and *V*-type, those where the steady-state catalytic rate constant (k_{cat}) is altered, the specific kinetic steps affected can vary depending on the enzyme^{13,17–19}. For instance, in *Mycobacterium tuberculosis* α -isopropylmalate synthase, the rate-limiting step changes from product release to chemistry upon allosteric inhibition

¹School of Biology, Biomedical Sciences Research Complex, University of St Andrews, St Andrews KY16 9ST, UK. ²Science for Life Laboratory, Department of Chemistry – BMC, Uppsala University, S-751 23 Uppsala, Sweden. ³School of Chemistry and Biochemistry, Georgia Institute of Technology, 901 Atlantic Drive NW, Atlanta, GA 30332, USA. ✉ e-mail: lynn.kamerlin@kemi.uu.se; rgds@st-andrews.ac.uk

by leucine¹⁷. The role of protein dynamics in allostery has been much less controversial when discussed in terms of conformational changes to promote physical events such as substrate binding and product release, or the interconversion rate among conformations^{11,20}. However, in systems where allosteric regulation affects the rate of the chemical step itself^{17–19}, the intersection at which local and remote protein motions, active-site electrostatic preorganisation, and ultimately catalysis meet remains challenging to pinpoint, despite recent advances toward this goal with Kemp eliminase^{5,21}.

ATP phosphoribosyltransferase (ATPPRT) (EC 2.4.2.17) catalyses the Mg^{2+} -dependent formation of *N*¹-(5-phospho- β -D-ribose)-ATP (PRATP) and inorganic pyrophosphate (PP_i) from ATP and 5-phospho- α -D-ribose 1-pyrophosphate (PRPP) (Fig. 1a), the first and flux-controlling step of histidine biosynthesis, and is allosterically inhibited by histidine in a negative feedback control loop^{22,23}. ATPRT is the focus of synthetic biology efforts to enable the production of histidine in bacteria^{16,24} and a promising drug target against some pathogenic bacteria^{25–27}. Short-form ATPRTs form an intricate allosteric system comprising catalytic (HisG_S) and regulatory (HisZ) subunits assembled as a hetero-octamer with a tetrameric core of HisZ sandwiched by two dimers of HisG_S^{28–33}. HisG_S on its own is catalytically active and insensitive to inhibition by histidine^{28,34}. Binding of HisZ, which has no catalytic power of its own, to form the ATPRT holoenzyme allosterically activates catalysis by HisG_S^{26,28,31,34}. However, HisZ also harbours the pocket where histidine binds and allosterically inhibits ATPRT. Thus, the regulatory protein plays a dual role, as allosteric activator of catalysis in the absence of histidine and mediator of allosteric inhibition in the presence of histidine^{19,31,33}.

In *Psychrobacter arcticus* ATPRT (*Pa*ATPPRT), structural and functional data indicate allosteric activation of catalysis triggered by HisZ (*Pa*HisZ) binding specifically perturbs the chemical step of the reaction taking place at the HisG_S (*Pa*HisG_S) active site located ~23 Å from the nearest *Pa*HisG_S:*Pa*HisZ interface^{18,29}. First, crystal structures

of the Michaelis complexes of the activated, hetero-octameric holoenzyme (henceforth referred to as *Pa*ATPPRT) and of the non-activated, dimeric enzyme (henceforth referred to as *Pa*HisG_S) showed Arg56 of one of the catalytic subunits reaching across the dimer interface to form a salt-bridge with the pyrophosphate moiety of PRPP in the active site of the other subunit (Fig. 1b) in the *Pa*ATPPRT structure but not in the *Pa*HisG_S structure. Therefore, allosteric activation was proposed to lead to more efficient leaving group departure at the transition state by stabilisation of the negative charge build-up on the pyrophosphate upon nucleophilic attack of ATP N1 on PRPP C1²⁹. Second, no burst in product formation was observed for the reaction catalysed by *Pa*HisG_S, and the multiple-turnover, pre-steady-state rate constant was in agreement with k_{cat} , suggesting chemistry is rate limiting in the nonactivated enzyme reaction. In contrast, a burst was observed in the reaction catalysed by *Pa*ATPPRT, producing a rate constant (k_{burst}) much higher than k_{cat} , supporting a mechanism where allosteric activation speeds up the chemical step, making product release rate limiting¹⁸. Finally, replacement of Mg^{2+} by Mn^{2+} , which more efficiently offsets the negative charge at the transition state, led to an ~3-fold enhancement of *Pa*HisG_S k_{cat} , as would be predicted, qualitatively, for a rate-limiting chemical step, but had no effect on *Pa*ATPPRT k_{cat} , where chemistry was already much faster than subsequent steps¹⁸.

As expected, an R56A-*Pa*HisG_S mutant had a reduced reaction rate in the nonactivated enzyme as measured at a fixed concentration of substrates, since R56 was posited to be important for leaving group departure in *Pa*HisG_S as well, only less efficiently. Intriguingly, upon *Pa*HisZ binding to R56A-*Pa*HisG_S, part of the activity was recovered²⁹. Here we employed site-directed mutagenesis, differential scanning fluorimetry (DSF), enzyme kinetics, ³¹P-NMR spectroscopy, protein crystallography, and molecular dynamics (MD) simulations to dissect this phenomenon, reveal that other single- and double-mutations at the *Pa*HisG_S active site display similar behaviour, and demonstrate

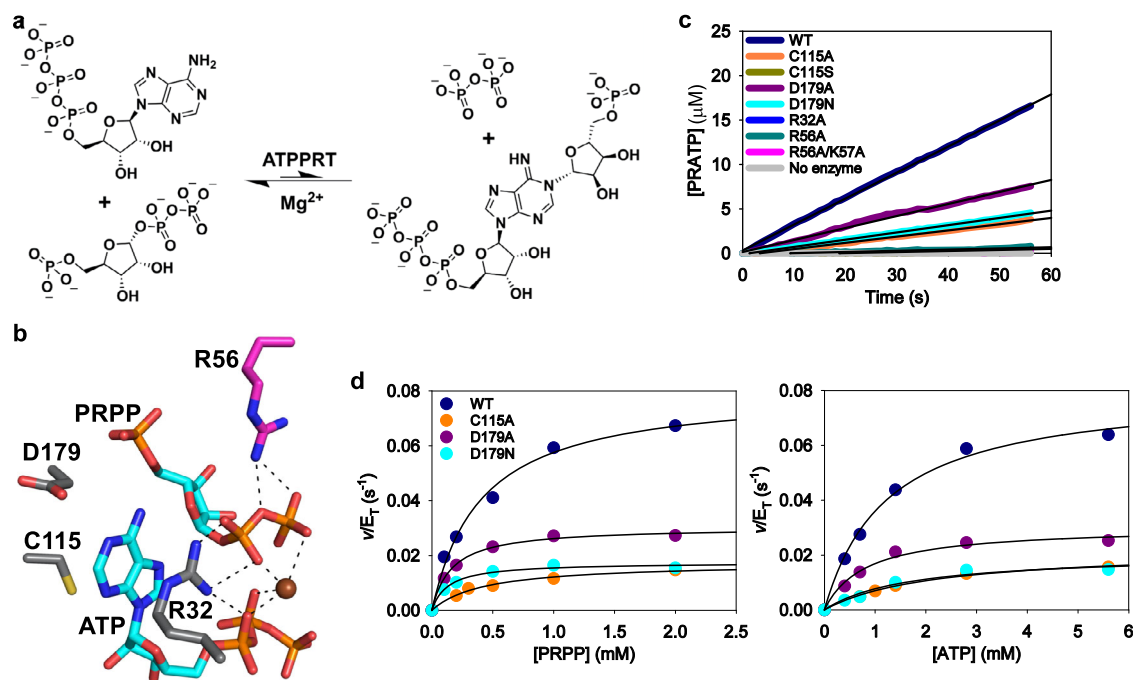


Fig. 1 | The effect of active-site mutations on *Pa*HisG_S. **a** The reversible, Mg^{2+} -dependent reaction catalysed by ATPRT. **b** Stick model of the active site of *Pa*ATPPRT (PDB ID 6FU2)²⁹. Oxygen is shown in red, nitrogen in blue, phosphorus in orange, sulphur in yellow, and carbon in either cyan (substrates), grey (in one of the *Pa*HisG_S subunits) or magenta (in the other *Pa*HisG_S subunit). Polar interactions are depicted as dashed lines, and the Mg^{2+} as sphere. **c** Representative traces of PRATP

formation time course catalysed by 5 μ M *Pa*HisG_S variants. Black lines are linear regressions of the data. Source data are provided as a Source Data file. **d** Substrate saturation curves for WT and mutant *Pa*HisG_S. Data are the mean of two independent measurements. Lines are best fit of the data to Eq. (1). Source data are provided as a Source Data file.

how modulation of *PaHisG₅* dynamics by *PaHisZ* propagates to the active site to affect the chemical step.

Results

C115A-, D179A-, and D179N-*PaHisG₅* are catalytically active

To assess the importance of active-site residues in catalysis, we introduced single and double mutations into the *PaHisG₅* amino acid sequence by site-directed mutagenesis of the *PaHisG₅*-coding sequence and expressed and purified the mutant proteins (Supplementary Fig. 1). Electrospray ionisation/time-of-flight-mass spectrometry (ESI/TOF-MS) confirmed the molecular masses of WT-, C115A-, C115S-, D179A-, R32A-, R56A-, and R56A/K57A-*PaHisG₅* variants were in agreement with the predicted values (Supplementary Fig. 2). The introduction of the D179N mutation was confirmed by MS/MS analysis of tryptic fragments (Supplementary Fig. 2). In an initial activity screen, reactions were monitored for just under 1 min by the continuous and direct UV/VIS absorbance-based assay for ATPPRT activity^{18,35} at fixed PRPP and ATP concentrations sufficient to saturate WT-*PaHisG₅*. PRATP formation was readily detected with C115A-, D179A-, D179N-, and WT-*PaHisG₅* (Fig. 1c), and linear regression of the data yielded apparent rate constants shown in Supplementary Table 1.

Substrate saturation curves for WT-, C115A-, D179A-, and D179N-*PaHisG₅* obeyed Michaelis-Menten kinetics (Fig. 1d), and data fit to Eq. (1) produced the apparent steady-state kinetic parameters in Supplementary Table 2. The Michaelis constant for ATP (K_{ATP}) increased less than 2-fold for C115A-*PaHisG₅*, and the Michaelis constant for PRPP (K_{PRPP}) actually decreased between 2- and 3-fold for D179A- and D179N-*PaHisG₅*, suggesting C115 and D179 make negligible contributions to substrate binding. The k_{cat} values for the mutants were reduced only ~4-fold in comparison with the WT-*PaHisG₅*, pointing to these residues' modest importance in catalysis. Over the course of the ATPPRT-catalysed reaction, the 6-NH₂ group must donate a proton to yield the 6-NH group of PRATP, and in the case of *PaATP*PRT, this proton abstraction happens on the enzyme¹⁸. Based on their respective positions in the active site (Fig. 1b)²⁹, both C115 and D179 were candidates to act as general base for this proton abstraction, but the small catalytic effect of their replacements for residues that cannot participate in acid-base catalysis does not support such role, leaving the identity of the general base still elusive.

C115S-, R32A-, R56A-, and R56A/K57A-*PaHisG₅* are catalytically compromised

No PRATP formation could be detected above the background noise of the assay (no-enzyme control) during the initial activity screen when either C115S-, R32A-, R56A-, or R56A/K57A-*PaHisG₅* was used as catalyst (Fig. 1c), indicating these mutants have impaired catalytic activity. DSF-based thermal denaturation assays showed these mutants display similar thermal unfolding profiles to the WT protein (Fig. 2a), demonstrating the mutations do not thermally destabilise the tertiary structure of the protein, and data fit to Eq. (2) yielded melting temperatures (T_m) shown in Supplementary Table 3. Moreover, as described previously¹⁸ and repeated here for WT-*PaHisG₅*, the presence of PRPP increased the T_m of the mutants (Fig. 2a; Supplementary Table 3), indicating the catalytically impaired *PaHisG₅* variants can bind PRPP, in agreement with the ordered kinetic mechanism proposed for this enzyme^{18,29}. Analytical size-exclusion chromatography produced similar elution profiles for WT-, C115S-, R32A-, R56A-, and R56A/K57A-*PaHisG₅* (Supplementary Fig. 3), which includes the expected dimer²⁹ and a higher oligomeric state. An activity screen with longer reaction times and twice as much enzyme as in the initial screen, to allow more product to accumulate, demonstrated the catalytic ability of C115S-, R32A-, R56A-, and R56A/K57A-*PaHisG₅* is significantly diminished but not abolished (Fig. 2b).

Even though C115 is only modestly important for catalysis, its replacement by serine led to a 117-fold reduction in activity (Table 1), perhaps due to the introduction of a detrimental interaction. The activities of R32A- and R56A-*PaHisG₅* decreased 25- and 42-fold, respectively, in comparison with the WT-*PaHisG₅* (Table 1). This demonstrates the importance of these residues in *PaHisG₅* catalysis, possibly because R56 and R32 may contribute to leaving group departure at the transition state^{18,29}. K57 is adjacent to R56 in the *PaHisG₅* primary sequence, but in all *PaHisG₅* and *PaATP*PRT crystal structures, it points away from the active site^{19,28,29}. We hypothesised that in the absence of the R56 guanidinium group, the K57 ϵ -NH₃⁺ group could move towards the active site and assist in leaving group departure. However, the R56A/K57A-*PaHisG₅* double mutant displayed a 254-fold decrease in activity (Table 1), which is only ~6-fold more catalytically impaired than the R56A-*PaHisG₅*, indicating just a modest catalytic importance for K57. R32, R56, K57, and C115 are highly conserved in *HisG₅* across species, and D179 is also conserved but sometimes replaced with a glutamate residue²⁹. Nevertheless, out of these five residues in *PaHisG₅*, only the arginine residues seem to be significantly important for catalysis.

PaHisZ allosterically rescues C115S-, R32A-, R56A-, and R56A/K57A-*PaHisG₅* catalysis

To assess the extent to which these mutations were also detrimental to *PaATP*PRT catalysis, and how much of the R56A-*PaHisG₅* activity could be recovered in the presence of *PaHisZ*²⁹, the effect of *PaHisZ* on the reaction catalysed by the impaired *PaHisG₅* mutants was determined. The regulatory protein surprisingly led to activation of all catalytically impaired *PaHisG₅* mutants (Fig. 2c), and data fit to Eq. (3) resulted in the apparent equilibrium dissociation constants (K_D) for *PaHisZ* displayed in Table 2. No activity was detected when the *PaHisG₅* mutant-catalysed reactions were carried out in the presence of bovine serum albumin (BSA) (Supplementary Fig. 4), ruling out that allosteric rescue was due to nonspecific protein binding. To gather orthogonal evidence for the allosteric rescue, the reaction catalysed by each *PaHisG₅* mutant was analysed by ³¹P-NMR spectroscopy in the presence and absence of *PaHisZ* (Supplementary Fig. 5) under conditions where product can be detected with WT-*PaHisG₅*¹⁸. The characteristic chemical shift at -3.30 ppm (Fig. 2d) previously assigned to the phosphorus in the *N*¹-5-phospho- β -D-ribose moiety of PRATP^{28,29}, was only detected here when *PaHisZ* was present in the reaction, confirming the rescue of the catalytically compromised mutants by the regulatory protein.

Substrate saturation curves for WT-, C115S-, R32A-, R56A-, and R56A/K57A-*PaATP*PRT obeyed Michaelis-Menten kinetics (Fig. 2e), and data fit to Eq. (1) produced the apparent steady-state kinetic parameters shown in Table 2, with the concentrations of each *PaATP*PRT variant calculated from the K_D for *PaHisZ* using Eq. (4). *PaHisZ* allosterically restored most of the catalytic activity of the impaired *PaHisG₅* mutants. In comparison with the WT-*PaATP*PRT, K_{PRPP} was unaltered by the mutations, and K_{ATP} increased by a maximum of 4-fold. The k_{cat} decreased by less than 2-fold for C115S-*PaATP*PRT as compared with WT-*PaATP*PRT (it is possible *PaHisZ* binding allosterically disrupts a putative catalytically detrimental interaction involving S115), and by less than 4-fold and 6-fold for R32A- and R56A-*PaATP*PRT. Only R56A/K57A-*PaATP*PRT k_{cat} was reduced by more than one order of magnitude (~14-fold) in comparison with WT-*PaATP*PRT, which is still a small effect in comparison with the 254-fold catalytic impairment of R56A/K57A-*PaHisG₅*.

Due to the long TEVP-cleavage time and low yield of the *PaHisZ* recovered, along with the extensive use of the regulatory protein in this work, a His-tagged *PaHisZ* was purified and employed from this point onwards. The apparent steady-state kinetic parameters (Supplementary Fig. 6) are very similar whether or not the His-tagged *PaHisZ* was used. Histidine binds to *PaHisZ* and allosterically inhibits *PaATP*PRT catalysis, and the suppression of the burst in product formation in the presence of histidine suggests that allosteric inhibition

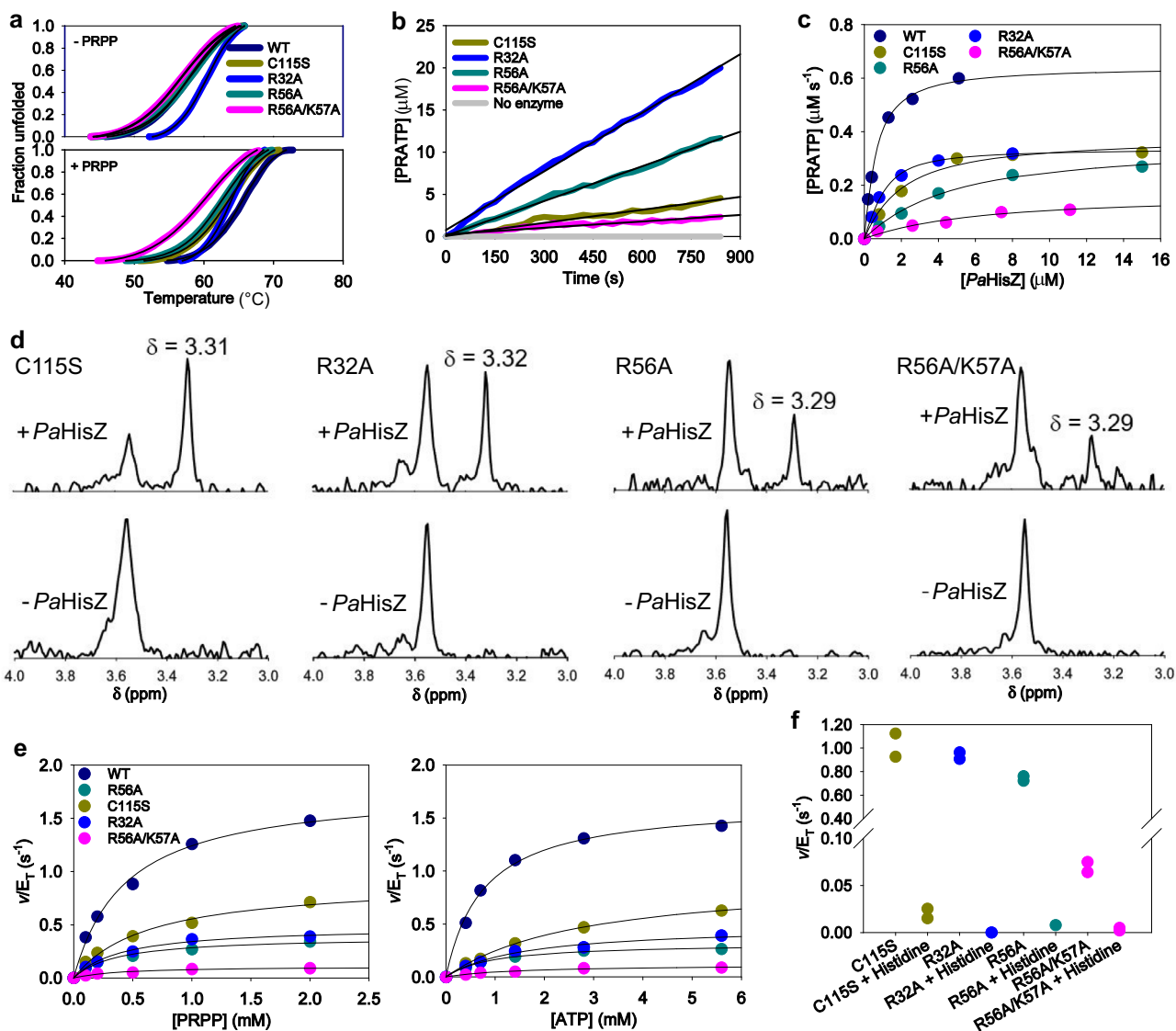


Fig. 2 | Allosteric rescue of catalytically impaired *PaHisG₅* mutants by *PaHisZ*. **a** DSF-based thermal denaturation of C115S-, R32A-, R56A-, or R56A/K57A-*PaHisG₅*. Traces are averages of three independent measurements. Lines of best fit to Eq. (2) are in black. Source data are provided as a Source Data file. **b** PRATP formation time course catalysed by 10 μM *PaHisG₅* variants. Traces are averages of two independent measurements. Black lines are linear regressions of the data. Source data are provided as a Source Data file. **c** Dependence of rate of reaction catalysed by *PaHisG₅* variants on the concentration of *PaHisZ*. Data are the mean of two independent measurements. Lines are best fit of the data to Eq. (3). Source data are

provided as a Source Data file. **d** Close-ups of the 4.0–3.0 ppm region of the ^{31}P -NMR spectra of the reaction catalysed by *PaHisG₅* mutants in the presence and absence of *PaHisZ*. The peak at -3.30 ppm corresponds to the phosphorus in the N^5 -5-phospho- β -D-ribose moiety of PRATP^{28,29}. Source data are provided as a Source Data file. **e** Substrate saturation curves for WT and mutant *PaATPRT*. Data are the mean of two independent measurements. Lines are best fit of the data to Eq. (1). Source data are provided as a Source Data file. **f** Effect of 1 mM histidine on mutant *PaATPRT*-catalysed reaction. Two independent measurements were carried out, and all data points are shown. Source data are provided as a Source Data file.

directly affects the chemical step of the reaction¹⁹. Histidine also inhibits the reaction catalysed by the rescued *PaATPRT* mutants (Fig. 2f; Supplementary Fig. 7), indicating the allosteric pathway responsible for inhibition is intact in these mutants.

Table 1 | Apparent rate constants (mean \pm fitting error) for *PaHisG₅* mutants from reactions monitored for 840 s

<i>PaHisG₅</i>	v/E_T (s^{-1})	Catalytic impairment ^a
C115S	0.0005 ± 0.0001	117-fold
R32A	0.0023 ± 0.0001	25-fold
R56A	0.0014 ± 0.0001	42-fold
R56A/K57A	0.00023 ± 0.00005	254-fold

^aRatio of v/E_T for WT-*PaHisG₅* (0.0586 ± 0.0002) to v/E_T reported here.

Allosteric activation of WT- and R56A-*PaHisG₅* by an orthologous *HisZ*

PaHisZ and *PaHisG₅* share 43% and 69% sequence identity with their orthologues from the pathogenic bacterium *Acinetobacter baumannii*, *AbHisZ* and *AbHisG₅*, respectively, but *PaHisZ* has been shown to be a potent allosteric inhibitor of *AbHisG₅*²⁶. We thus hypothesised that *AbHisZ* could inhibit WT-*PaHisG₅*. However, addition of *AbHisZ* activated catalysis by WT-*PaHisG₅* (Fig. 3a), and data fit to Eq. (3) yielded an apparent K_D for *AbHisZ* of $9 \pm 1 \mu\text{M}$. Moreover, *AbHisZ* also rescued catalysis by R56A-*PaHisG₅* (Fig. 3a), but their interaction involved positive co-operativity as evidenced by the sigmoidal dependence of the reaction rate on the regulatory protein. The R56A-*PaHisG₅* mutant was chosen due to its significant catalytic impairment and the proposed role in catalysis for R56. The data were fit to Eq. (5), yielding a concentration of *AbHisZ* at the inflection point ($K_{0.5}$) and a Hill

Table 2 | Apparent steady-state kinetic parameters (mean±fitting error) for PaATPPRT variants (all mutations are in PaHisG₅)

PaATPPRT	PaHisZ K _D (μM)	k _{cat} (s ⁻¹)	K _{PRPP} (mM)	K _{ATP} (mM)	Activation by PaHisZ ^a
WT	0.44 ± 0.05	1.72 ± 0.07	0.44 ± 0.05	0.76 ± 0.07	29-fold
C115S	1.7 ± 0.4	0.93 ± 0.05	0.6 ± 0.1	2.8 ± 0.2	1,860-fold
R32A	0.49 ± 0.06	0.48 ± 0.04	0.41 ± 0.06	1.5 ± 0.3	208-fold
R56A	4.0 ± 0.6	0.35 ± 0.05	0.37 ± 0.04	0.9 ± 0.1	250-fold
R56A/K57A	5 ± 2	0.12 ± 0.01	0.4 ± 0.1	1.5 ± 0.3	521-fold

^aRatio of k_{cat} reported here to v/E_T from Supplementary Table 1 (WT) and Table 1 (mutants).

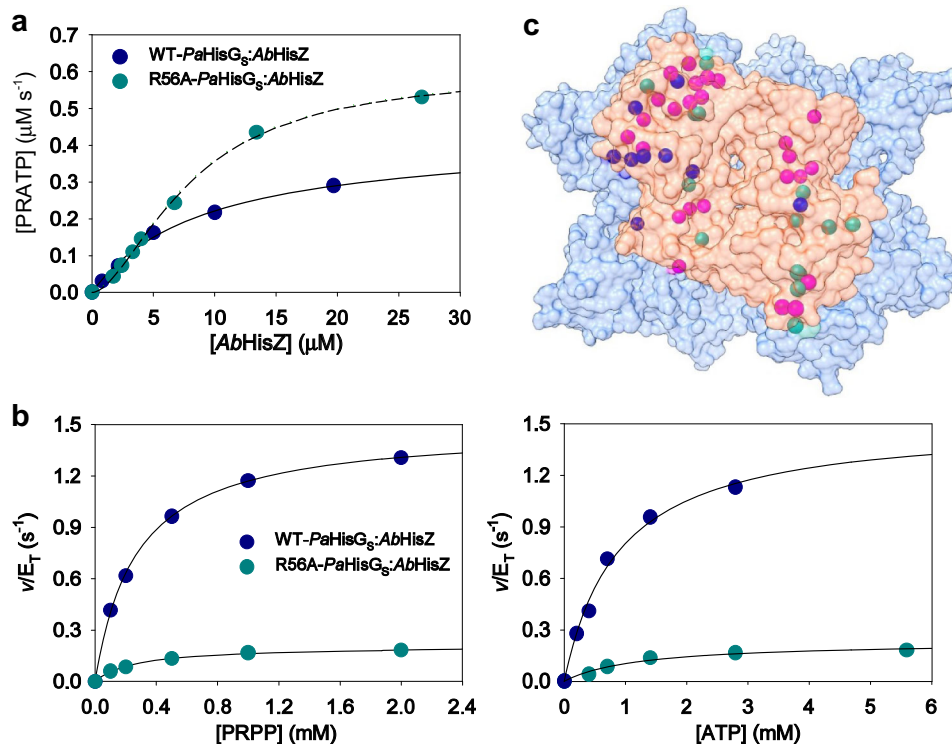


Fig. 3 | Allosteric activation of PaHisG₅ variants by AbHisZ. **a** Dependence of rate of reaction catalysed by PaHisG₅ variants on the concentration of AbHisZ. Data are the mean of two independent measurements. Best fit of the data to Eq. (3) is shown as a solid line. Best fit of the data to Eq. (5) is shown as a dashed line. Source data are provided as a Source Data file. **b** Substrate saturation curves for WT-PaHisG₅/AbHisZ and R56A-PaHisG₅/AbHisZ. Data are the mean of two independent measurements. Lines are best fit of the data to Eq. (1). WT-PaHisG₅/AbHisZ concentration was calculated from the K_D for AbHisZ with Eq. (4), while R56A-PaHisG₅/AbHisZ

concentration was assumed to be the same as R56A-PaHisG₅ in the presence of 26 μM AbHisZ. Source data are provided as a Source Data file. **c** The crystal structure of PaATPPRT²⁸ (PDB ID 5M8H) viewed from above the PaHisG₅ dimer. PaHisG₅ (orange) and PaHisZ (blue) are in surface rendering. The Ca atoms of specific PaHisZ residues at the interface with PaHisG₅ are shown as spheres, with pink depicting identical residues to AbHisZ, blue depicting residues with similar properties to those in AbHisZ, and green, those not conserved in AbHisZ.

coefficient (*h*) of $8.1 \pm 0.4 \mu\text{M}$ and 1.68 ± 0.08 , respectively. Nonetheless, this fit is intended only to highlight the sigmoidal behaviour of the data, since the experiment could not be carried out under pseudo-first-order conditions, i.e. [R56A-PaHisG₅] - [AbHisZ] in the experiment; thus, Eq. (5) does not hold.

Substrate saturation curves for WT-PaHisG₅/AbHisZ and R56A-PaHisG₅/AbHisZ hybrid complexes obeyed Michaelis-Menten kinetics (Fig. 3b), and data fit to Eq. (1) produced the following apparent k_{cat}, K_{PRPP}, and K_{ATP}: $1.49 \pm 0.02 \text{ s}^{-1}$, $0.27 \pm 0.01 \text{ mM}$, and $0.9 \pm 0.1 \text{ mM}$ for WT-PaHisG₅/AbHisZ; $0.22 \pm 0.02 \text{ s}^{-1}$, $0.27 \pm 0.02 \text{ mM}$, and $1.2 \pm 0.3 \text{ mM}$ for R56A-PaHisG₅/AbHisZ. These values are in good agreement with those for WT- and R56A-PaATPPRT (Table 2), indicating AbHisZ recapitulates the catalytic activation of PaHisG₅ to a similar extent the native PaHisZ does. Furthermore, AbHisZ is capable of efficiently relaying the histidine inhibition allosteric signal to WT- and R56A-PaHisG₅ (Supplementary Fig. 8). We mapped the PaHisZ residues at the interface between the PaHisG₅ dimer and the PaHisZ tetramer in the

PaATPPRT hetero-octamer²⁸ (Fig. 3c), and found that 25 of those are strictly conserved in AbHisZ. It is possible that these residues have an important role in transmitting the allosteric signal for both activation and inhibition.

Crystal structures of R56A-PaHisG₅ and R56A-PaATPPRT

In an attempt to gain insight into the effect of the R56A mutation at the atomic level, we solved the crystal structures of both R56A-PaHisG₅ and R56A-PaATPPRT bound to PRPP:ATP. Refinement statistics are summarised in Supplementary Table 4, and the electron-density maps for PRPP:ATP in both structures are shown in Supplementary Fig. 9. Even WT-PaHisG₅ and WT-PaATPPRT are known to form the Michaelis complex *in crystallo*, likely due to a highly unfavourable on-enzyme equilibrium for the forward reaction^{18,29}. The active site interactions are very similar between the two structures, except the electron density for Mg²⁺ in R56A-PaATPPRT was not well defined, so the metal was not modelled in, and the hydrogen bond between E163 and the PRPP 3'-OH

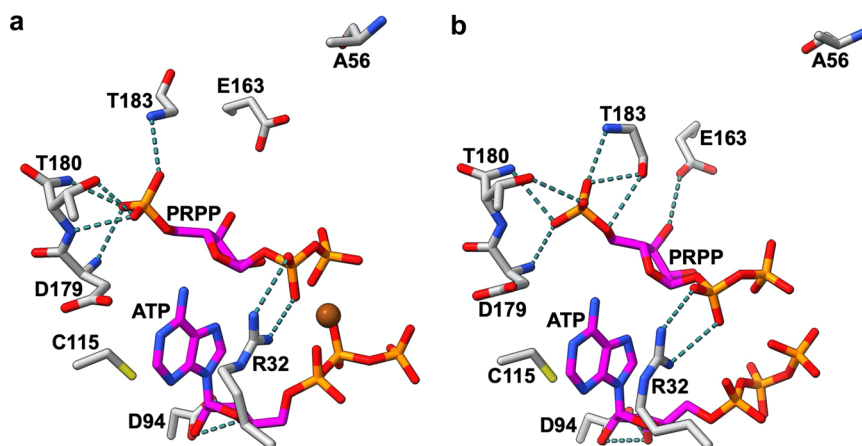


Fig. 4 | Crystal structures of R56A-*PaHisG₅* and R56A-*PaATPPRT* bound to PRPP:ATP. a Stick model of the active site of R56A-*PaHisG₅*. **b** Stick model of the active site of R56A-*PaATPPRT*. In both panels, oxygen is shown in red, nitrogen in blue, phosphorus in orange, sulphur in yellow, and carbon in either magenta

(substrates) or grey (protein). The A56 side chain is contributed by the adjacent *PaHisG₅* subunits. Polar interactions are depicted as dashed lines, and the Mg²⁺ as a sphere.

is absent in R56A-*PaHisG₅* (Fig. 4). The structures are also very similar to those of the respective WT enzymes²⁹. Therefore, any structural or conformational differences that may lead to allosteric rescue of R56A-*PaHisG₅* catalysis are not captured in the static view of the crystal structure.

PaHisZ binding alters *PaHisG₅* dynamics

MD simulations were performed on the WT-*PaHisG₅*:PRPP:ATP complex both in the presence and absence of the regulatory protein *PaHisZ* in order to gain insight into the role of *PaHisZ* in the allosteric modulation of *PaHisG₅*. We then constructed dynamic cross-correlation matrices (DCCM) for the C α -atoms during simulations of each system (Supplementary Fig. 10) to analyze the occurrence of correlated motions in the nonactivated and activated dimers for both WT and R56A variants. These plots show a clear shift in the *PaHisG₅* dimer conformational ensemble upon allosteric activation, with increases in both correlated and anti-correlated motions compared to the nonactivated dimer, and similar effects upon activation of both the wild-type enzyme and the R56A variant. Spearman's rank correlation coefficients between the nonactivated and activated systems are 0.26 for WT-*PaHisG₅* and 0.37 for R56A-*PaHisG₅*. In contrast, the coefficients between WT-*PaHisG₅* and R56A-*PaHisG₅* in each of the nonactivated and activated states are 0.86 and 0.84, respectively. This suggests high similarity between WT-*PaHisG₅* and R56A-*PaHisG₅* when the two systems are in the same state (nonactivated *vs.* activated), but low similarity between the nonactivated and activated states of each individual variant. It is expected that external structural perturbations (such as ligand binding or, in this case, the binding of *PaHisZ* to *PaHisG₅*) would alter such conformational fluctuations, as has been observed in other allosteric systems^{36–38}, and it can also be seen here that *PaHisZ* binding increases order in the system.

The conformational behavior of the activated dimer was further explored using the shortest path map (SPM) approach as implemented by Osuna and coworkers³⁹, which enables the identification of pairs of residues in both the active site and distal positions⁴⁰ with the highest contributions to the communication pathways in nonactivated and activated *PaHisG₅*. As described by Osuna⁴¹ and Guo and Zhou⁴² in the implementation we have used, the shortest path lengths are computed using the Dijkstra algorithm⁴³ by going through all nodes of the graph to identify the shortest path from the first to the last protein residue. This allows the identification of which edges of the graph are shorter (i.e. more correlated, see Supplementary Tables 5–7) and more frequently used for going through all residues of the protein. All edges are

then normalized, and only those edges having the largest contributions are represented in the SPM. Comparison of the computed SPM in the nonactivated and activated enzymes (Fig. 5a, b) illustrates that *PaHisZ* binding increases intermonomer communication pathways across the two subunits of the *PaHisG₅* dimer, which could be expected to in turn facilitate key interactions between R56 and PRPP across the dimer. This is in overall agreement with the allosteric activation mechanism gleaned from the crystal structures of *PaHisG₅* and *PaATPPRT*²⁹. Furthermore, when also considering interactions between the dimer and the regulatory protein (Fig. 5c, d), it can be seen that the SPM spans one of the *PaHisZ* subunits, bridges both monomers of *PaHisG₅* and communicates with the regulatory protein mainly through helices α 7,8 of *PaHisZ* and β 4,5,11 of *PaHisG₅* (Supplementary Fig. 11). Interestingly, the calculated SPM (Fig. 5d) contains V257, G268 and I269 of the histidine-binding loop of *PaHisZ* (D256–I269)¹⁹, suggesting a perturbation of the allosteric communication pathway upon histidine binding.

To identify residues that have the largest effect on allosteric signal communication, we have performed node-weakening analysis by removing the nodes corresponding to the residues located at the interface between *PaHisG₅* and *PaHisZ*, where the SPM goes through both proteins (5 nodes on *PaHisG₅* and 7 nodes on *PaHisZ*), and calculating the change in CPL (characteristic path length) upon removal of each node (Supplementary Table 8)^{44–46}. We then selected the three residues displaying the highest impact on the Δ CPL and performed molecular dynamic simulations of four selected *in-silico* mutants of *PaATPPRT* (Y105A-*PaHisG₅*, Y105F-*PaHisG₅*, N185A-*PaHisZ*, and K186D-*PaHisZ*), with the aim of disrupting the communication pathway between *PaHisG₅* and *PaHisZ*. When comparing the SPM of the WT-*PaATPPRT* with those of the various mutants we generated *in-silico*, we see that the pathway is slightly reorganized without displaying critical changes that disrupt the communication signal between the two proteins (Supplementary Fig. 12). These results are in line with a proposal that allosteric activation is due to a global “nesting” effect of *PaHisZ* over *PaHisG₅*, with a preferred but not unique allosteric activation pathway.

We also analyzed the contribution of each residue to the overall protein dynamics by means of the dynamical flexibility indices (DFI)⁴⁷ which measure the dynamic response at each residue in a protein when the system is perturbed (e.g. by a random Brownian kick). This mimics the natural condition in a crowded cellular environment, where the protein is exposed to many different random forces. Thus, the DFI analysis aims to capture the contribution of each position in the protein to the underlying functional dynamics, highlighting the key

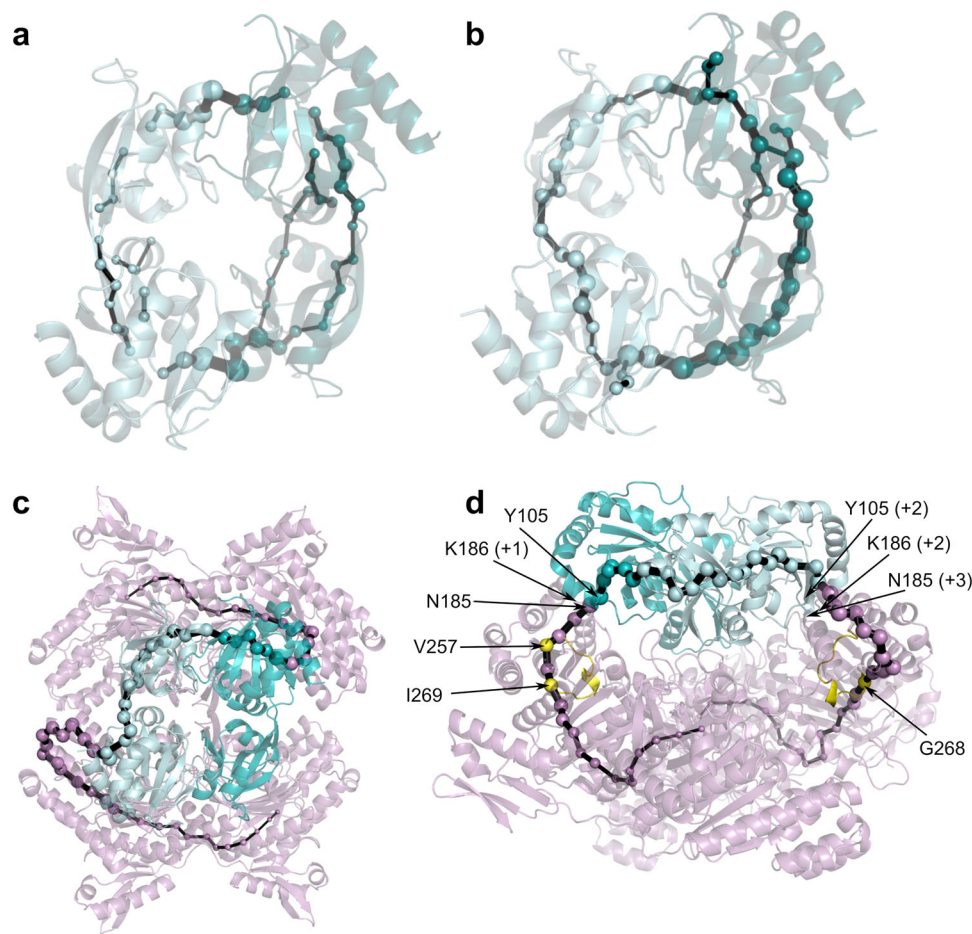


Fig. 5 | Effect of *PaHisZ* binding on *PaHisG₅* dynamic network. **a** SPM analysis of nonactivated *PaHisG₅* dimer. **b** SPM analysis of activated *PaHisG₅* dimer upon *PaHisZ* binding (only the catalytic subunits are shown). **c** SPM analysis of *PaATPPRT* including *PaHisZ* residues. **d** Side view (90° rotation) of **c**. *PaHisG₅* monomers are shown in light and dark teal, while *PaHisZ* is shown in pink. The histidine-binding loop (D256 – I269) is shown in yellow in **d**. The sizes of the edges (black lines) and

vertices (spheres) indicate the strength of the network (the larger size the more pathways available, and thus the higher the importance for allosteric communication). The positions of key residues in the histidine-binding loop and some included in the node-weakening analysis are denoted by arrows; if they are adjacent to the SPM, the number in brackets indicates how many amino-acid residues away they are from the closest residue encompassed by the SPM.

residues and regions that mediate functionally important dynamical information. Our analysis (Supplementary Fig. 13) reveal *PaHisZ* binding changes the DFI of *PaHisG₅* compared with nonactivated *PaHisG₅*, in particular at the helices inferred to be important for communication at the *PaHisG₅-PaHisZ* interface from the SPM analysis (Fig. 5), as well as the region containing R32 and R56.

Insights into the dynamics of allosteric rescue of R56A-*PaHisG₅*

Additional MD simulations were performed on both nonactivated and activated R56A-*PaHisG₅*:PRPP:ATP complexes to gather knowledge at the atomic level into the allosteric rescue of this variant. Given the catalytic importance of R32 and R56 and their hypothesized involvement in facilitating leaving group departure, we tracked the distance between C ζ of each side chain and P α of the PP_i moiety of PRPP during our simulations (Fig. 6a). It can be gleaned from the data that the R56 side chain displays a bimodal distribution of distances in WT-*PaHisG₅* (Fig. 6b). This distribution comprises a peak at -4.4 Å corresponding to a catalytic conformation in which this side chain forms a salt-bridge with the PRPP PP_i moiety, and another at -7.8 Å, corresponding to a non-catalytic rotamer of this residue. Binding of *PaHisZ* shifts the distance distribution towards the catalytically active rotamer (Fig. 6c). This furnishes support for *PaHisZ* binding constraining the conformational dynamics of *PaHisG₅*, fostering a preorganized active

site in which the R56 guanidinium group is poised to help stabilize the leaving group at the transition state.

Changes in R32 distance distribution upon allosteric activation of WT-*PaHisG₅* are more subtle, but follow a similar trend as seen for R56, with a peak at -5.4 Å in WT-*PaHisG₅* (Fig. 6d) shifting to one at -4.2 Å in WT-*PaATPPRT* (Fig. 6e) to favor interaction with the PP_i moiety. This effect is exacerbated in the absence of R56, where a broad distribution of R32 distances in R56A-*PaHisG₅* (Fig. 6f) changes to a very narrow peak at -4.2 Å in R56A-*PaATPPRT* (Fig. 6g). These simulations offer a dynamics-based hypothesis for the allosteric rescue of R56A-*PaHisG₅*: in the absence of R56, *PaHisZ* binding constrains the conformational ensemble of R56A-*PaHisG₅* mainly to a population where a very narrow distribution of R32 rotamers is sampled that is optimized for a salt-bridge with the PP_i leaving group at the transition state, partially offsetting the loss of such interaction with R56. It is also tempting to speculate that allosteric rescue of R32A-*PaHisG₅* by *PaHisZ* might involve in turn a similar constraint of R56 dynamics to facilitate leaving group departure at the transition state and partially compensate for the loss of R32.

The R32A and R56A substitutions affect the chemical step

The proposal that allosteric rescue of R56A-*PaHisG₅*, and likely R32A-*PaHisG₅*, by *PaHisZ* is underpinned by constrained *PaHisG₅* protein

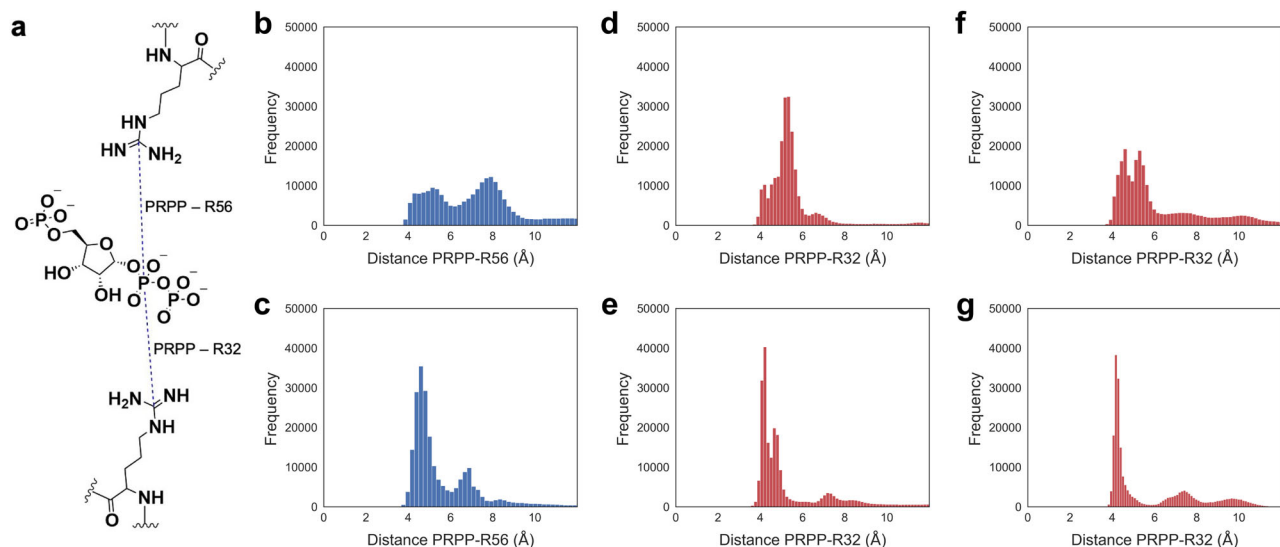


Fig. 6 | Effect of *PaHisZ* binding on *PaHisG₅* R56 and R32 rotamers. a Schematic rendering of the distances (dashed lines) between C γ of either R56 or R32 and P α of the PP $_i$ moiety of PRPP monitored during MD simulations, henceforth referred to as PRPP – R56 distance and PRPP – R32 distance, respectively. **b** Distribution of PRPP – R56 distances in WT-*PaHisG₅*. **c** Distribution of PRPP – R56 distances in WT-*PaATPPRT*. **d** Distribution of PRPP – R32 distances in WT-*PaHisG₅*. **e** Distribution of PRPP – R32 distances in WT-*PaATPPRT*. **f** Distribution of PRPP – R32 distances in R56A-*PaHisG₅*. **g** Distribution of PRPP – R32 distances in R56A-*PaATPPRT*.

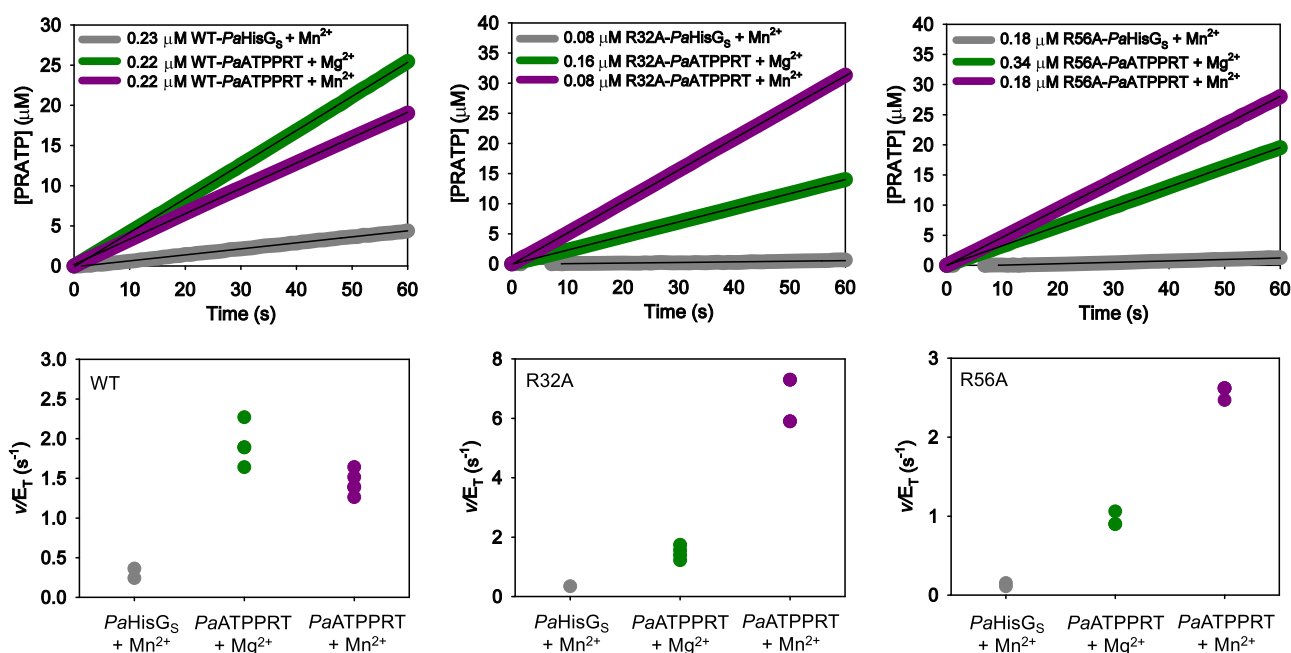


Fig. 7 | Effect of Mn^{2+} on R32A-*PaATPPRT* and R56A-*PaATPPRT* reactions. a PRATP formation time course catalysed by *PaHisG₅* and *PaATPPRT* variants at fixed, saturating concentration of PRPP and ATP. Traces are averages of two to four independent measurements. Black lines are linear regressions of the data. Source data are provided as a Source Data file. **b** Apparent first-order rate constants for *PaHisG₅* and *PaATPPRT* variants. All data points are shown. Two independent measurements were carried out for *PaHisG₅* variants, and four for *PaATPPRT*. For the latter, where less than four data points are apparent, identical rates for two replicates overlap.

dynamics restoring proper active-site electrostatic preorganisation predicts the rescued reaction rates must reflect at least in part the chemical step of the reaction. We have previously demonstrated that replacement of Mg^{2+} by Mn^{2+} increases WT-*PaHisG₅* k_{cat} , and density-functional theory calculations provided a rationale for this effect based on more efficient stabilisation of the negative charges by Mn^{2+} via d -orbital bonding to the oxygens of the departing PP $_i$ at the transition state¹⁸. This was corroborating evidence that chemistry was the rate-limiting step in *PaHisG₅* catalysis, but not in *PaATPPRT* where Mn^{2+} had

no significant impact on k_{cat} . This observation is reproduced here. At saturating concentrations of both substrates, Mn^{2+} allows product formation to be detected at a WT-*PaHisG₅* concentration too low to detect reaction with Mg^{2+} , but does not increase the WT-*PaATPPRT* reaction rate (Fig. 7). In contrast, when R32A-*PaATPPRT* and R56A-*PaATPPRT* reactions were carried out with Mn^{2+} instead of Mg^{2+} , the rate of product formation increased (Fig. 7a), and the apparent first-order rate constants increased by ~5-fold and ~3-fold, respectively, in comparison with those with Mg^{2+} (Fig. 7b). This indicates the rates of

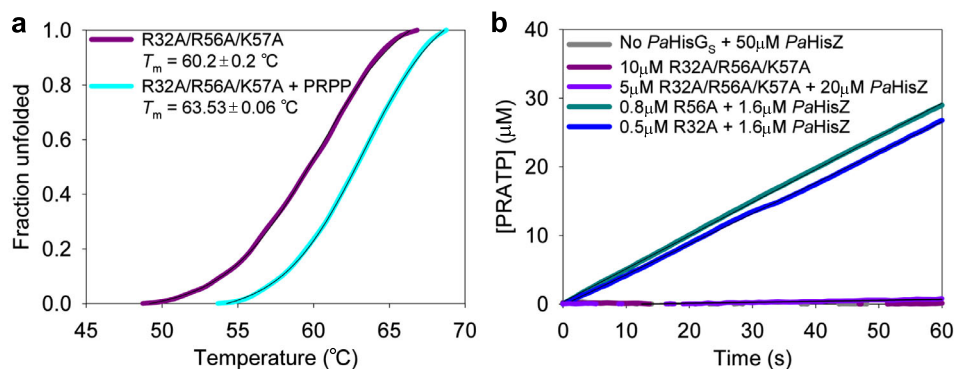


Fig. 8 | Biochemical characterisation of R32A/R56A/K57A-*PaHisG₅*. **a** DSF-based thermal denaturation of R32/R56A/K57A-*PaHisG₅*. Traces are averages of three independent measurements. Lines of best fit to Eq. (2) are in black. Source data are

provided as a Source Data file. **b** PRATP formation time course catalysed by *PaHisG₅* variants. Traces are averages of two independent measurements. Black lines are linear regressions of the data. Source data are provided as a Source Data file.

the rescued mutants reflect the chemical step of the reaction, i.e. unlike WT-*PaATPPRT*¹⁸, chemistry is at least partially rate-limiting for R32A-*PaATPPRT* and R56A-*PaATPPRT*. Interestingly, R32A-*PaATPPRT* and R56A-*PaATPPRT* apparent first-order rate constants with Mn^{2+} are even higher than the corresponding one for WT-*PaATPPRT*. However, these rate constants do not reflect the same reaction step. It is likely that Mn^{2+} enhances the rate of chemistry substantially for WT-*PaATPPRT*, but the observed rate constant is dominated by product release¹⁸. On the other hand, with R32A-*PaATPPRT* and R56A-*PaATPPRT*, the effect of Mn^{2+} is the enhancement of the rate of chemistry itself. Surprisingly, the apparent first-order rate constants for R32A-*PaHisG₅* and R56A-*PaHisG₅* with Mn^{2+} were measurable, $0.12 \pm 0.01 \text{ s}^{-1}$ and $0.13 \pm 0.01 \text{ s}^{-1}$, respectively, only -2.5-fold lower than that for WT-*PaHisG₅* with Mn^{2+} , although still very low in comparison with those for R32A-*PaATPPRT* (-54-fold higher) and R56A-*PaATPPRT* (-20-fold higher) (Fig. 7), suggesting the more efficient charge stabilisation ability of Mn^{2+} can partially rescue the activity of these mutants. This observation highlights the importance of electrostatic catalysis in this enzymatic reaction.

Given the proposed role of R56 in stabilising the departure of the negatively charged leaving group, the possibility that a lysine residue could replace R56 with similar catalytic ability was considered. To evaluate this possibility, R56K-*PaHisG₅* was produced. ESI/TOF-MS analysis resulted in the expected mass (Supplementary Fig. 14a), and DSF showed the mutation does not change the T_m of the protein (Supplementary Fig. 14b). At substrate concentrations saturating for WT-*PaHisG₅*, however, the R56K-*PaHisG₅* reaction rate is reduced -24-fold in comparison with the WT-*PaHisG₅*, and although there is an -11-fold activation in the presence of *PaHisZ*, the R56K-*PaATPPRT* reaction rate is still -2-fold lower compared with the nonactivated WT variant (Supplementary Fig. 14c). These observations indicate the amino group cannot substitute for the guanidinium group at position 56 of *PaHisG₅*. Furthermore, allosteric activation by *PaHisZ* cannot rescue catalysis in this case.

R32A/R56A/K57A-*PaHisG₅* cannot be rescued by *PaHisZ*

The hypothesis that R32 and R56 can compensate to a certain extent for the absence of the other in the presence of *PaHisZ* to restore the electrostatic preorganisation of *PaHisG₅* active site predicts that removal of both arginine residues would prevent allosteric rescue of catalysis. To test this prediction, the R32A/R56A/K57A-*PaHisG₅* triple mutant was produced (Supplementary Fig. 1) and ESI/TOF-MS analysis resulted in the expected mass (Supplementary Fig. 2). DSF indicated that the additional mutation does not alter the T_m of the protein (Fig. 8a) as compared with R56A/K57A-*PaHisG₅* or WT-*PaHisG₅* T_m . Furthermore, PRPP led to an increase in T_m , showing the triple mutant

can bind this substrate. As expected, PRATP formation could not be detected with R32A/R56A/K57A-*PaHisG₅* as catalyst (Fig. 8b). Upon addition of excess *PaHisZ*, some PRATP formation could be marginally detected above the assay background noise (Fig. 8b), demonstrating R32A/R56A/K57A-*PaATPPRT* still retains residual catalytic activity. However, the apparent rate constant is reduced -777-fold in comparison with that of WT-*PaATPPRT* (Supplementary Fig. 6), and -340-fold and -222-fold in comparison with those of R32A-*PaATPPRT* and R56A-*PaATPPRT*, respectively (Supplementary Fig. 15), in accordance with the proposed necessity for at least one of the two arginine residues to aid in leaving group departure for full catalytic power of *PaATPPRT*.

Discussion

Rescue of catalytically impaired enzyme mutants is well established, but not as observed for *PaATPPRT*. Chemical rescue by small molecules that mimic missing residue side chains is a useful tool to probe the function of active-site residues in catalysis⁴⁸, and a hyper-nucleophilic cholesterol analogue in which an -OOH group replaces the sterol -OH group could rescue the base-catalysed endoproteolytic activity of a mutant hedgehog protein where the catalytically essential aspartate general base was mutated to an alanine, which rendered the reaction highly impaired with the natural substrate⁴⁹. A catalytically compromised receptor tyrosine kinase carrying mutations in the activation loop tyrosine residues that would otherwise be autophosphorylated could be allosterically rescued by the juxtamembrane segment via autophosphorylation of this segment's Y687, but in this case the effect of the phospho-Y687 is exerted by direct interaction with arginine residues that normally interact with the phosphorylated tyrosine residues in the activation loop⁵⁰. In hetero-tetrameric tryptophan synthase, where catalysis by the β subunit is allosterically activated by the α subunit, the catalytically inactive E109A mutant of the β subunit could not be rescued by the α subunit, but the activity of the E109A- $\alpha_2\beta_2$ complex could be partially restored by CsCl, possibly by modulation of the conformational ensemble of the complex⁵¹. In human prolyl isomerase CypA, the second-shell S99T mutation, which is highly detrimental to catalysis, can be partially counteracted by additional mutations outside the active site which rescue the dynamics of interconversion between two essential conformations⁷.

PaATPPRT is unique because the rescue of catalytically compromised *PaHisG₅* mutants by *PaHisZ*, and even by the orthologous *AbHisZ*, is truly allosteric since the regulatory subunit binds far from the active site where the mutations exert a detrimental effect on transition state stabilisation. The narrowing of the distribution of states sampled by the *PaHisG₅* upon *PaHisZ* binding has a direct impact on the positioning and orientation of R32 and R56, which are better poised to facilitate leaving group departure by electrostatic

stabilisation of the PP_i negative charges. This implies allosteric activation of catalysis in *PaATPPRT* involves modulation of the conformational flexibility of the holoenzyme and electrostatic preorganisation of the active site. The catalytic recruitment of R32 and R56 in concert with Mg²⁺ to stabilise PP_i is reminiscent of that of arginine residues in adenylate kinase to promote phosphate transfer from ATP to AMP, where thermally equilibrated protein motions were also proposed to help achieve optimal electrostatic preorganisation⁵². Interestingly, replacement of a key arginine residue for a lysine was detrimental to catalysis in adenylate kinase as well⁵².

Another important aspect of the allosterically rescued R32A- and R56A-*PaATPPRT* is that k_{cat} is at least partially limited by the chemical step, a drastic change from WT-*PaATPPRT* in which k_{cat} is determined by product release¹⁸. Electrostatic preorganisation exerts its effect on catalysis at the chemical step, i.e. as the reaction progresses from the preorganised Michaelis complex to the transition state. Thus it is paramount that an experimentally measured rate constant purporting to reflect any coupling of protein motions to the preorganisation of the Michaelis complex be limited by the chemical step^{9,53}. This is what is observed with the allosteric rescue of the catalytically compromised mutants of *PaHisG_S*, establishing a direct connection between *PaHisZ*-modulated rotamers of R32 and R56 and electrostatic preorganisation of the active site, which is required for optimal catalysis.

Methods

Reagents

All commercially available chemicals were used without further purification. BaseMuncher endonuclease was purchased from AbCam. Ampicillin, dithiothreitol (DTT), isopropyl β-D-1-thiogalactopyranoside (IPTG) and 2-(*N*-morpholino)ethanesulfonic acid-sodium dodecyl sulfate (MES-SDS) were purchased from Formedium. DH5α chemically competent *Escherichia coli*, DpnI were purchased from New England Biolabs (NEB). QIAprep Spin Miniprep, PCR clean-up and Plasmid Midi kits were from Qiagen. Ethylenediaminetetraacetic acid (EDTA)-free Complete protease inhibitor cocktail was from Roche. ATP, C43(DE3) and BL21(DE3) chemically competent *E. coli*, D₂O, glycerol, histidine, imidazole, lysozyme, PRPP, potassium chloride, and tricine were purchased from Sigma-Aldrich. Agarose, dNTPs, kanamycin, 4-(2-hydroxyethyl)piperazine-1-ethanesulfonic acid (HEPES), MgCl₂, NaCl, PageRuler Plus Prestained protein ladder, PageRuler™ Plus Prestained protein ladder, and SYPRO orange protein gel stain were from ThermoFisher Scientific. DNA oligonucleotide primers were synthesised by Integrated DNA technologies (IDT).

Site-directed mutagenesis of *PaHisG_S*

Site-directed mutagenesis was carried out with overlapping primers according to the method of Liu and Naismith⁵⁴. Primer sequences are listed in Supplementary Table 9. For the triple mutant R32A/R56A/K57A-*PaHisG_S*, the R56A/K57A-*PaHisG_S* expression vector was used as DNA template. For all other mutants, WT-*PaHisG_S* expression vector was used. Correct insertion of each mutation was confirmed by DNA sequencing performed by either Eurofins Genomics or DNA Sequencing & Services at University of Dundee.

Protein expression and purification

PaHisG_S, *PaHisZ*, *Mycobacterium tuberculosis* pyrophosphatase (*MtPPase*), and tobacco etch virus protease (TEVP) were produced as previously described²⁸. *AbHisZ* was produced as previously reported²⁶. All *PaHisG_S* mutants were expressed and purified by the same protocol as *PaHisG_S*²⁸. His-tagged *PaHisZ* was purified by the same protocol as *PaHisZ* up to and including the first chromatography²⁸, after which fractions producing a single band at the expected MW in SDS-PAGE were pooled and dialysed against 2 × 2L of 20 mM HEPES pH 8.0, concentrated using 10,000 molecular weight cutoff (MWCO)

ultrafiltration membranes (Millipore), aliquoted and stored at -80 °C. His-tagged *PaHisZ*, C115A-, C115S-, D179A-, D179N-, R32A-, R56A-, R56A/K57A-, R56K, and R32A/R56A/K57A-*PaHisG* had their intact mass determined by ESI/TOF-MS, and D179N-*PaHisG_S* tryptic peptides underwent MS/MS analysis to confirm the mutation, all performed by the BSRC Mass-Spectrometry and Proteomics Facility at the University of St Andrews. The concentration of WT-*PaHisG_S*, WT-*PaHisZ*, *MtPPase* and TEVP was determined as published²⁸. The concentration of His-tagged *PaHisZ* and *PaHisG_S* mutants was determined spectrophotometrically (NanoDrop) at 280 nm based on the theoretical extinction coefficients (ϵ_{280}) calculated in the ProtParam tool of ExPASy: ϵ_{280} of 27,930 M⁻¹ cm⁻¹ for His-tagged *PaHisZ*; 8940 M⁻¹ cm⁻¹ for all *PaHisG_S* mutants.

DSF

DSF measurements (λ_{ex} = 490 nm, λ_{em} = 610 nm) were performed in 96-well plates on a Stratagene Mx3005p instrument. Reactions (50 μL) contained 100 mM tricine, 100 mM KCl, 15 mM MgCl₂, 4 mM DTT pH 8.5, 7 μM enzyme, and either 0 mM or 2 mM PRPP, with 5X Sypro Orange (Invitrogen) added to each well. Thermal denaturation curves were recorded over a temperature range of 25–93 °C with increments of 1 °C min⁻¹. Control curves lacked protein and were subtracted from curves containing protein. All measurements were carried out in triplicate.

Analytical size-exclusion chromatography

Analytical size-exclusion chromatography was performed on a Superdex 200 10/300 GL column (GE Healthcare) attached to a Bio-Rad NGC FPLC at 4 °C. WT-, C115S-, R32A-, R56A- and R56A/K57A-*PaHisG_S* (1 mg mL⁻¹, pre-incubated with DTT [2 mM]) were loaded onto the column (equilibrated with 20 mM HEPES pH 8.0) and eluted with 1 column volume of 20 mM HEPES pH 8.0 at 0.225 mL min⁻¹.

Enzyme activity assay

Unless stated otherwise, all reactions (500 μL) were carried out in 1 cm path-length quartz cuvettes under initial-rate conditions at 20 °C, and the increase in absorbance at 290 nm due to the formation of PRATP (ϵ_{290} = 3600 M⁻¹ cm⁻¹)³⁵ was monitored for 60 s in a Shimadzu UV-2600 spectrophotometer in 100 mM tricine, 100 mM KCl, 15 mM MgCl₂, 4 mM DTT, pH 8.5, 10 μM *MtPPase*, and various concentrations of PRPP and ATP. Cuvettes were incubated in the spectrophotometer at 20 °C for 3 min before reaction was initiated by the addition of PRPP. Control reactions lacked enzyme.

Activity of *PaHisG_S* mutants in the absence of *PaHisZ*

Activity of C115A-, C115S-, D179A-, D179N-, R32A-, R56A-, and R56A/K57A-*PaHisG* (5 μM) was assayed for 60 s in the presence of 5.6 mM ATP and 2 mM PRPP. WT-*PaHisG_S* (5 μM) was included in as a positive control. Additionally, the activity of C115S-, R32A-, R56A- and R56A/K57A-*PaHisG* (10 μM) was assayed for 870 s in the presence of 5.6 mM ATP and 2 mM PRPP. Exceptionally, activity of R56K-*PaHisG* (6 μM) was assayed both in the absence and presence of *PaHisZ* (20 μM).

Determination of apparent K_D for *PaHisZ*, His-tagged *PaHisZ* and *AbHisZ*

Initial velocities were measured in 5.6 mM ATP and 2 mM PRPP. For *PaHisZ* K_D , 0.42 μM WT-, 0.59 μM C115A-, 1.1 μM R32A-, 1.1 μM R56A- and 1.7 μM R56A/K57A-*PaHisG_S* were assayed in the presence of varying concentrations of *PaHisZ* (0–5.1 μM for WT-*PaHisG_S*; 0–15 μM for C115S-*PaHisG_S*; 0–8 μM for R32A-*PaHisG_S*; 0–15 μM for R56A-*PaHisG_S*; and 0–11 μM for R56A/K57A-*PaHisG_S*). For His-tagged *PaHisZ* K_D , 0.23 μM WT-, 0.49 μM R32A-, and 0.79 μM R56A-*PaHisG_S* were assayed in the presence of varying concentrations of His-tagged-*PaHisZ* (0–1.6 μM). For *AbHisZ* K_D , 0.19 μM WT- and 2.5 μM R56A-*PaHisG_S* were assayed in the presence of varying concentration of *AbHisZ* (0–19.7 μM

for WT-*PaHisG_S*; 0–26.9 μM for R56A-*PaHisG_S*). Alternatively, 1 μM C115S-, 1 μM R32A-, 1 μM R56A-, and 1.6 μM R56A/K57A-*PaHisG_S* were assayed in the presence of 20 μM BSA.

WT-, C115A-, D179A- and D179N-*PaHisG_S* saturation kinetics

Initial rates for 3.4 μM WT-, 10.1 μM C115A-, 9.2 μM D179A- and 10.0 μM D179N-*PaHisG_S* were measured at saturating concentrations of one substrate (either 2 mM PRPP or 5.6 mM ATP) and varying concentrations of the other, either ATP (0–5.6 mM) or PRPP (0–2 mM).

C115S-, R32A-, R56A- and R56A/K57A-*PaATPPRT* saturation kinetics

Initial rates for 0.4 μM WT-, 0.5 μM C115S-, 0.9 μM R32A-, 0.9 μM R56A-, and 1.2 μM R56A/K57A-*PaATPPRT* were measured at saturating concentrations of one substrate (either 2 mM PRPP or 5.6 mM ATP) and varying concentrations of the other, either ATP (0–5.6 mM) or PRPP (0–2 mM). Alternatively, initial rates for 0.22 μM WT-*PaATPPRT* with His-tagged *PaHisZ* replacing *PaHisZ* were measured at saturating concentration of one substrate (with 2 mM PRPP or 2.8 mM ATP) and varying concentrations of the other, either ATP (0–2.8 mM) or PRPP (0–2 mM).

WT- and R56A-*PaHisG_S*/*AbHisZ* saturation kinetics

Initial rates for 0.26 μM WT-, and 2.5 μM R56A-*PaHisG_S*/*AbHisZ* (the latter was assumed from the concentrations of 2.5 μM R56A-*PaHisG_S* and 19.7 μM *AbHisZ*) were measured at saturating concentrations of one substrate (either 2 mM PRPP or 2.8 mM ATP for WT- and 5.6 mM for R56A-*PaHisG_S*/*AbHisZ*) and varying concentrations of the other, either ATP (0–2.8 mM for WT-; 0–5.6 mM for R56A-*PaHisG_S*/*AbHisZ*) or PRPP (0–2 mM). For WT-*PaHisG_S*/*AbHisZ*, background rates of control reactions lacking *AbHisZ* were subtracted.

Inhibition by histidine

Initial rates for 0.43 μM C115S-, 0.49 μM R32A-, 0.79 μM R56A-, and 2.6 μM R56A/K57A-*PaHisG_S* with either 3.2 μM His-tagged *PaHisZ* (for C115S-, R32A-, and R56A-*PaHisG_S*) or 6.4 μM His-tagged *PaHisZ* (for R56A/K57A-*PaHisG_S*) were measured at saturating concentrations of both substrates (2 mM PRPP and 5.6 mM ATP) in the presence and absence of 1 mM histidine. Initial rates for 0.26 μM WT-, and 2.5 μM R56A-*PaHisG_S*/*AbHisZ* (the latter was assumed from the concentrations of 2.5 μM R56A-*PaHisG_S* and 19.7 μM *AbHisZ*) were measured at saturating concentrations of both substrates (2 mM PRPP and either 2.8 mM ATP for WT- or 5.6 mM for R56A-*PaHisG_S*/*AbHisZ*) in the presence and absence of 1 mM histidine.

³¹P-NMR spectra of the *PaHisG_S* and *PaATPPRT* reactions

In 500 μL reactions, either 10 μM R56A-, 10 μM C115S-, 20 μM R32A- or 20 μM R56A/K57A-*PaHisG_S* was incubated in the presence or absence of 30 μM *PaHisZ* in 100 mM tricine, 100 mM KCl, 15 mM MgCl₂, 4 mM DTT, pH 8.5, 20 μM *MtPPase*, 2 mM PRPP and 5.6 mM ATP for 1 h at 20 °C. Proteins were removed by passage through 10,000 MWCO Vivaspin centrifugal concentrators, after which 100 μL of D₂O was added to each sample. ³¹P-NMR spectra were recorded on either a Bruker AV 400 or Bruker AVII 400 spectrometer, and a total of 128 scans were collected for each sample.

Activity of R32A/R56A/K57A-*PaHisG_S*

R32A/R56A/K57A-*PaHisG_S* (10 μM in the absence of His-tagged *PaHisZ* and 5 μM in the presence of 20 μM His-tagged *PaHisZ*) was assayed for catalytic activity under initial-rate conditions in the presence of 5.6 mM ATP and 2 mM PRPP. R32A- and R56A-*PaHisG_S* (0.5 μM and 0.8 μM , respectively) in the presence of 1.6 μM His-tagged *PaHisZ* were assayed as positive controls for allosteric rescue. Negative controls contained 50 μM His-tagged *PaHisZ* but lacked *PaHisG_S*.

WT-, R32A- and R56A-*PaATPPRT* activities with Mn²⁺

Initial rates were determined for 0.23 μM WT-*PaHisG_S*, 0.22 μM WT-*PaATPPRT*, 0.08 μM R32A-*PaHisG_S*, 0.08 μM R32A-*PaATPPRT*, 0.18 μM R56A-*PaHisG_S*, and 0.18 μM R56A-*PaATPPRT* in 100 mM tricine, 100 mM KCl, 15 mM MnCl₂, 4 mM DTT, pH 8.5 and 10 μM *MtPPase* at saturating concentrations of ATP (1.4 mM for WT enzymes; 5.6 mM for mutant enzymes) and PRPP (1 mM for WT enzymes; 2 mM for mutant enzymes). Initial rates were also determined for 0.22 μM WT-*PaATPPRT*, 0.16 μM R32A-*PaATPPRT*, and 0.34 μM R56A-*PaATPPRT* in 100 mM tricine, 100 mM KCl, 15 mM MgCl₂, 4 mM DTT, pH 8.5 and 10 μM *MtPPase* at saturating concentrations of ATP (5.6 mM) and PRPP (2 mM).

Crystallisation, X-ray data collection and data processing

Crystals of R56A-*PaHisG_S* were grown, soaked in PRPP and ATP and stored as described for WT-*PaHisG_S*²⁹, whereas crystals of R56A-*PaATPPRT* were grown as described for WT-*PaATPPRT*²⁸ and soaked in PRPP and ATP and stored as described for WT-*PaATPPRT*²⁹. X-ray diffraction data for R56A-*PaHisG_S* were collected in house as previously reported²⁸ and processed with iMosflm⁵⁵, while data for R56A-*PaATPPRT* were collected at Diamond Light Source (UK) and processed at the automated processing pipeline at Diamond with Xia2⁵⁶ integrated with DIALS⁵⁷. R56A-*PaHisG_S* and R56A-*PaATPPRT* structures were solved by molecular replacement in MOLREP using WT-*PaHisG_S*:PRPP:ATP (PDB ID: 6FCT) and WT-*PaATPPRT*:PRPP:ATP (PDB ID: 6FU2)²⁹ structures, respectively, as search models. Structures were refined using cycles of model building with COOT⁵⁸ and refinement with Refmac⁵⁹. ATP was modelled at either 70% or 80% occupancy in R56A-*PaATPPRT*.

MD simulations

Molecular dynamics simulations were performed on WT-*PaHisG_S*:PRPP:ATP (PDB ID: 6FCT)²⁹, WT-*PaATPPRT*:PRPP:ATP (PDB ID: 6FU2)²⁹, R56A-*PaHisG_S*:PRPP:ATP (PDB ID: 7Z8U), and R56A-*PaATPPRT*:PRPP:ATP (PDB ID: 7Z6R). Any missing regions in the structures were reconstructed using Modeller v. 9.23⁶⁰. In the case of *PaHisZ*, these were reconstructed using the lowest energy conformation prediction combined with visual inspection; in other systems, *PaHisG_S* was used as a template (as well as for modeling the position of the binding site magnesium ions). A distal extra Mg²⁺ was deleted from R56A-*PaHisG_S*:PRPP:ATP structure. Finally, the adenine moiety of ATP was flipped into a catalytically productive conformation in all the starting structures. Protonation states of all titratable residues were determined based on a combination of empirical screening using PROPKA v3.1⁶¹, and visual inspection of the local environment. The E122, E163 and H103 side chains were predicted to be found in their ionized states. Previously prepared WT-*PaATPPRT*:PRPP:ATP was used as starting point to introduce, *in silico*, the point mutations from the node-weakening analysis: Y105A-*PaHisG_S*, Y105F-*PaHisG_S*, N185A-*PaHisZ*, and K186D-*PaHisZ*. Corresponding rotamers were selected using the Dunbrack 2010 Rotamer Library⁶².

Partial charges for the ligand PRPP were calculated *in vacuo* at the HF/6-31G* level of theory using Gaussian 16 Rev. A.03⁶³, and fitted using the standard restrained electrostatic potential (RESP) protocol as implemented in Antechamber⁶⁴ (Supplementary Table 10). All other force field terms for PRPP were then described using the Amber force field ff14SB⁶⁵ together with revised parameters to describe bioorganic phosphates⁶⁶. The parameters for ATP were taken from the literature⁶⁷. We used an octahedral cationic dummy model to describe Mg²⁺, following from previous successful results using this model^{68,69}.

All MD simulations were performed using the GPU-accelerated version of Amber16⁷⁰, with the protein and water molecules described

using the amber force field ff14SB⁶⁵ and the TIP3P⁷¹ water model, respectively. All systems were solvated in an octahedral box of water molecules, extended 8 Å from the closest solute molecule in every direction. Each system was neutralized by adding Na⁺ or Cl⁻ counterions to ensure overall charge neutrality. Counterions were placed using the “addions” approach as implemented in Amber16⁷⁰. The dimeric and hetero-octameric forms of the enzyme were simulated for 10 × 500 ns and 5 × 500 ns, respectively, in the NPT ensemble. The solvated systems were first minimized using 5000 steps of steepest descent minimization with 500 kcal mol⁻¹ Å⁻² positional restraints placed on all solute atoms to minimize all hydrogen atoms and solvent molecules, followed by 5000 steps of conjugate gradient minimization, with the restraint dropped to 5 kcal mol⁻¹ Å⁻². The minimized system was then heated from 0 to 300 K in an NVT ensemble over 250ps of simulation time using the Berendsen thermostat⁷² with a time constant of 1ps for the coupling while maintaining the 5 kcal mol⁻¹ Å⁻² restraint. The restraint was then limited to heavy atoms of the substrates for a further 200ps of NPT equilibration, followed by 200ps of unrestrained equilibration. After minimization, five distance restraints were applied during the simulations to PRPP and ATP (four to PRPP and one to ATP) to prevent dissociation of the substrates from the active site throughout the MD simulations (see Supplementary Table 11 for a full list of the restraints applied). Note that no restraints were applied between the substrate and any of the regions of interest to ensure full conformational freedom of such regions.

All production-quality simulations were performed using a 2 fs time step, with the SHAKE algorithm⁷³ used to constrain all bonds containing hydrogen atoms. Temperature and pressure were controlled by the Langevin thermostat with a collision frequency of 1ps⁻¹⁷⁴, and the Berendsen barostat with a 1 ps coupling constant⁷². A cutoff of 8 Å was applied to all non-bonded interactions, with the long range electrostatics being evaluated using the particle mesh Ewald (PME) approach⁷⁵. The root mean square deviations (RMSD) of all backbone atoms for each system during the production runs is shown in Supplementary Fig. 16. Unless stated otherwise, all analysis was performed using CPPTRJ⁷⁶. Principal Component Analysis was performed in Cartesian coordinate space on the Cα atoms of the shared dimeric region of all the studied systems, by first root-mean-square fitting all the trajectories to the WT-*PaHisG_S* crystal structure. DCCMs were generated with Bio3D⁷⁷. Two-sided Spearman’s rank order correlation tests were used to measure the monotonicity of the relationship between distinct correlation matrices. The upper triangle of each 416 × 416 matrix was used, representing a sample size of $n = 86,528$. The standard assumptions (data measured on an interval scale, and the two variables are monotonically related) were used.

Kinetics and thermal denaturation data analysis

Kinetic and thermal denaturation data were analysed by the nonlinear regression function of SigmaPlot 14.0 (SPSS Inc.). Data points with error bars represent mean ± SEM of two to four independent measurements, and kinetic and equilibrium constants are given as mean ± fitting error. Alternatively, all data points were plotted. Substrate saturation curves at a fixed concentration of the co-substrate were fitted to Eq. (1). Thermal denaturation data were fitted to Eq. (2). Initial rate data at varying concentrations of HisZ were fitted to either Eqs. (3) or (5). The concentration of ATPPRT at any concentration of *PaHisG_S* and either *PaHisZ* or *AbHisZ* was calculated according to Eq. (4). In Eqs. 1 – 5, k_{cat} is the steady-state turnover number, ν is the initial rate, E_T is total enzyme concentration, K_M is the apparent Michaelis constant, S is the concentration of the varying substrate, V_{max} is the maximal velocity, F_U is fraction unfolded, T is the temperature in °C, T_m is the melting temperature, c is the slope of the transition region,

and LL and UL are folded and unfolded baselines, respectively, h is the Hill coefficient, $K_{0.5}$ is the concentration of *AbHisZ* at the inflection point, G is the concentration of *PaHisG_S*, Z is the concentration of either *PaHisZ* or *AbHisZ*, K_D^{app} is the apparent equilibrium dissociation constant, and $ATPPRT$ is the concentration of either *PaATPPRT* of *PaHisG_S/AbHisZ* complex.

$$\frac{\nu}{E_T} = \frac{k_{cat}S}{K_M + S} \quad (1)$$

$$F_U = LL + \frac{UL - LL}{1 + e^{(T_m - T)/c}} \quad (2)$$

$$\nu = V_{max} \frac{G + Z + K_D^{app} - \sqrt{(G + Z + K_D^{app})^2 - 4GZ}}{2G} \quad (3)$$

$$ATPPRT = \frac{G + Z + K_D^{app} - \sqrt{(G + Z + K_D^{app})^2 - 4GZ}}{2} \quad (4)$$

$$\nu = \frac{V_{max}Z^h}{K_{0.5} + Z^h} \quad (5)$$

Reporting summary

Further information on research design is available in the Nature Portfolio Reporting Summary linked to this article.

Data availability

Structure factor amplitudes and coordinates for the crystal structures of R56A-*PaHisG_S*:PRPP:ATP and R56A-*PaATPPRT*:PRP-P:ATP were deposited to the Protein Data Bank under accession numbers 7Z8U and 7Z6R, respectively. MD simulations were based on coordinates for WT-*PaHisG_S*:PRPP:ATP and WT-*PaATPPRT*:PRPP:ATP downloaded from the Protein Data Bank under accession numbers 6FCT and 6FU2, respectively. All protein mass spectrometry data were deposited to FigShare under DOIs <https://doi.org/10.6084/m9.figshare.19658367> (D179N-*PaHisG_S* tryptic digestion analysis) and <https://doi.org/10.6084/m9.figshare.19658229> (intact mass analysis for remaining *PaHisG_S* variants). Parameters used to describe the ligands and the magnesium dummy model, input files, starting structures, topologies and snapshots from our molecular dynamics simulations are available for download from Zenodo under <https://doi.org/10.5281/zenodo.7077771> [<https://zenodo.org/record/7077771#.Y2pZReTPID8>]. Source data are provided with this paper.

References

- Goodey, N. M. & Benkovic, S. J. Allosteric regulation and catalysis emerge via a common route. *Nat. Chem. Biol.* **4**, 474–482 (2008).
- Hammes, G. G., Benkovic, S. J. & Hammes-Schiffer, S. Flexibility, diversity, and cooperativity: pillars of enzyme catalysis. *Biochemistry* **50**, 10422–10430 (2011).
- Kern, D. & Zuiderweg, E. R. The role of dynamics in allosteric regulation. *Curr. Opin. Struct. Biol.* **13**, 748–757 (2003).
- Warshel, A. et al. Electrostatic Basis for Enzyme Catalysis. *Chem. Rev.* **106**, 3210–3235 (2006).
- Otten, R. et al. How directed evolution reshapes the energy landscape in an enzyme to boost catalysis. *Science* **370**, 1442–1446 (2020).
- Silva, R. G., Murkin, A. S. & Schramm, V. L. Femtosecond dynamics coupled to chemical barrier crossing in a Born-Oppenheimer enzyme. *Proc. Natl Acad. Sci.* **108**, 18661–18665 (2011).

7. Otten, R. et al. Rescue of conformational dynamics in enzyme catalysis by directed evolution. *Nat. Commun.* **9**, 1314 (2018).
8. Pudney, C. R. et al. Fast protein motions are coupled to enzyme H-transfer reactions. *J. Am. Chem. Soc.* **135**, 2512–2517 (2013).
9. Warshel, A. & Bora, R. P. Perspective: Defining and quantifying the role of dynamics in enzyme catalysis. *J. Chem. Phys.* **144**, 180901 (2016).
10. Schramm, V. L. & Schwartz, S. D. Promoting vibrations and the function of enzymes. emerging theoretical and experimental convergence. *Biochemistry* **57**, 3299–3308 (2018).
11. Pisco, J. P. et al. Uncoupling conformational states from activity in an allosteric enzyme. *Nat. Commun.* **8**, 203 (2017).
12. Fan, Y., Cross, P. J., Jameson, G. B. & Parker, E. J. Exploring modular allostery via interchangeable regulatory domains. *Proc. Natl Acad. Sci.* **115**, 3006–3011 (2018).
13. Pedreno, S., Pisco, J. P., Larrouy-Maumus, G., Kelly, G. & de Carvalho, L. P. Mechanism of feedback allosteric inhibition of ATP phosphoribosyltransferase. *Biochemistry* **51**, 8027–8038 (2012).
14. Pádua, R. A. P. et al. Mechanism of activating mutations and allosteric drug inhibition of the phosphatase SHP2. *Nat. Commun.* **9**, 4507 (2018).
15. Buller, A. R. et al. Directed evolution of the tryptophan synthase beta-subunit for stand-alone function recapitulates allosteric activation. *Proc. Natl Acad. Sci.* **112**, 14599–14604 (2015).
16. Schendzielorz, G. et al. Taking control over control: use of product sensing in single cells to remove flux control at key enzymes in biosynthesis pathways. *ACS Synth. Biol.* **3**, 21–29 (2014).
17. Casey, A. K., Schwalm, E. L., Hays, B. N. & Frantom, P. A. V-type allosteric inhibition is described by a shift in the rate-determining step for α -isopropylmalate synthase from *Mycobacterium tuberculosis*. *Biochemistry* **52**, 6737–6739 (2013).
18. Fisher, G. et al. Allosteric activation shifts the rate-limiting step in a short-form ATP phosphoribosyltransferase. *Biochemistry* **57**, 4357–4367 (2018).
19. Thomson, C. M., Alphey, M. S., Fisher, G. & da Silva, R. G. Mapping the structural path for allosteric inhibition of a short-form ATP phosphoribosyltransferase by histidine. *Biochemistry* **58**, 3078–3086 (2019).
20. Pacholarz, K. J. et al. Hybrid mass spectrometry approaches to determine how l-histidine feedback regulates the enzyme MtATP-phosphoribosyltransferase. *Structure* **25**, 730–738 (2017).
21. Bunzel, H. A. et al. Evolution of dynamical networks enhances catalysis in a designer enzyme. *Nat. Chem.* **13**, 1017–1022 (2021).
22. Ames, B. N., Martin, R. G. & Garry, B. J. The first step of histidine biosynthesis. *J. Biol. Chem.* **236**, 2019–2026 (1961).
23. Martin, R. G. The First Enzyme in Histidine Biosynthesis: The nature of feedback inhibition by histidine. *J. Biol. Chem.* **238**, 257–268 (1963).
24. Kulis-Horn, R. K., Persicke, M. & Kalinowski, J. *Corynebacterium glutamicum* ATP-phosphoribosyl transferases suitable for L-histidine production-Strategies for the elimination of feedback inhibition. *J. Biotechnol.* **206**, 26–37 (2015).
25. Cho, Y., Ioerger, T. R. & Sacchettini, J. C. Discovery of novel nitro-benzothiazole inhibitors for *Mycobacterium tuberculosis* ATP phosphoribosyl transferase (HisG) through virtual screening. *J. Med. Chem.* **51**, 5984–5992 (2008).
26. Read, B. J. et al. Allosteric inhibition of *Acinetobacter baumannii* ATP phosphoribosyltransferase by protein:dipeptide and protein:protein interactions. *ACS Infect. Dis.* **8**, 197–209 (2022).
27. Moggre, G. J., Poulin, M. B., Tyler, P. C., Schramm, V. L. & Parker, E. J. Transition state analysis of adenosine triphosphate phosphoribosyltransferase. *ACS Chem. Biol.* **12**, 2662–2670 (2017).
28. Stroek, R. et al. Kinetics and structure of a cold-adapted hetero-octameric ATP phosphoribosyltransferase. *Biochemistry* **56**, 793–803 (2017).
29. Alphey, M. S. et al. Catalytic and anticatalytic snapshots of a short-form ATP phosphoribosyltransferase. *ACS Catal.* **8**, 5601–5610 (2018).
30. Bovee, M. L., Champagne, K. S., Demeler, B. & Francklyn, C. S. The quaternary structure of the HisZ-HisG N-1-(5'-phosphoribosyl)-ATP transferase from *Lactococcus lactis*. *Biochemistry* **41**, 11838–11846 (2002).
31. Champagne, K. S., Sissler, M., Larrabee, Y., Doublet, S. & Francklyn, C. S. Activation of the hetero-octameric ATP phosphoribosyl transferase through subunit interface rearrangement by a tRNA synthetase paralog. *J. Biol. Chem.* **280**, 34096–34104 (2005).
32. Sissler, M. et al. An aminoacyl-tRNA synthetase paralog with a catalytic role in histidine biosynthesis. *Proc. Natl Acad. Sci.* **96**, 8985–8990 (1999).
33. Vega, M. C. et al. Regulation of the hetero-octameric ATP phosphoribosyl transferase complex from *Thermotoga maritima* by a tRNA synthetase-like subunit. *Mol. Microbiol.* **55**, 675–686 (2005).
34. Livingstone, E. K., Mittelstadt, G., Given, F. M. & Parker, E. J. Independent catalysis of the short form HisG from *Lactococcus lactis*. *FEBS Lett.* **590**, 2603–2610 (2016).
35. Smith, D. W. & Ames, B. N. Phosphoribosyladenosine monophosphate, an intermediate in histidine biosynthesis. *J. Biol. Chem.* **240**, 3056–3063 (1965).
36. Popovych, N., Sun, S., Ebright, R. H. & Kalodimos, C. G. Dynamically driven protein allostery. *Nat. Struct. Mol. Biol.* **13**, 831–838 (2006).
37. Agoni, C., Ramharack, P. & Soliman, M. E. S. Allosteric inhibition induces an open WPD-loop: a new avenue towards glioblastoma therapy. *RSC Adv.* **8**, 40187–40197 (2018).
38. Townsend, P. D. et al. The role of protein-ligand contacts in allosteric regulation of the *Escherichia coli* catabolite activator protein. *J. Biol. Chem.* **290**, 22225–22235 (2015).
39. Romero-Rivera, A., Garcia-Borràs, M. & Osuna, S. Role of conformational dynamics in the evolution of retro-aldolase activity. *ACS Catal.* **7**, 8524–8532 (2017).
40. Maria-Solano, M. A., Kinatader, T., Iglesias-Fernández, J., Sterner, R. & Osuna, S. In silico identification and experimental validation of distal activity-enhancing mutations in tryptophan synthase. *ACS Catal.* **11**, 13733–13743 (2021).
41. Osuna, S. The challenge of predicting distal active site mutations in computational enzyme design. *WIREs Comput. Mol. Sci.* **11**, e1502 (2021).
42. Guo, J. & Zhou, H.-X. Protein allostery and conformational dynamics. *Chem. Rev.* **116**, 6503–6515 (2016).
43. Dijkstra, E. W. A note on two problems in connexion with graphs. *Numer. Math.* **1**, 269–271 (1959).
44. Wang, W. et al. Dynamics correlation network for allosteric switching of PreQ1 riboswitch. *Sci. Rep.* **6**, 31005 (2016).
45. Sethi, A., Eargle, J., Black, A. A. & Luthey-Schulten, Z. Dynamical networks in tRNA:protein complexes. *Proc. Natl Acad. Sci.* **106**, 6620–6625 (2009).
46. Rehman, A. U. et al. Decoding allosteric communication pathways in protein lysine acetyltransferase. *Int. J. Biol. Macromol.* **149**, 70–80 (2020).
47. Nevin Gerek, Z., Kumar, S. & Banu Ozkan, S. Structural dynamics flexibility informs function and evolution at a proteome scale. *Evol. Appl.* **6**, 423–433 (2013).
48. Toney, M. D. & Kirsch, J. F. Direct Brønsted analysis of the restoration of activity to a mutant enzyme by exogenous amines. *Science* **243**, 1485–1488 (1989).
49. Ciulla, D. A., Jorgensen, M. T., Giner, J. L. & Callahan, B. P. Chemical bypass of general base catalysis in Hedgehog protein cholesterolysis using a hyper-nucleophilic substrate. *J. Am. Chem. Soc.* **140**, 916–918 (2018).
50. Plaza-Menacho, I. et al. RET functions as a dual-specificity kinase that requires allosteric inputs from juxtamembrane elements. *Cell Rep.* **17**, 3319–3332 (2016).

51. Ruvinov, S. B., Ahmed, S. A., McPhie, P. & Miles, E. W. Monovalent cations partially repair a conformational defect in a mutant tryptophan synthase alpha 2 beta 2 complex (beta-E109A). *J. Biol. Chem.* **270**, 17333–17338 (1995).
52. Kerns, S. J. et al. The energy landscape of adenylate kinase during catalysis. *Nat. Struct. Mol. Biol.* **22**, 124–131 (2015).
53. Loveridge, E. J., Behiry, E. M., Guo, J. & Allemann, R. K. Evidence that a ‘dynamic knockout’ in *Escherichia coli* dihydrofolate reductase does not affect the chemical step of catalysis. *Nat. Chem.* **4**, 292–297 (2012).
54. Liu, H. & Naismith, J. H. An efficient one-step site-directed deletion, insertion, single and multiple-site plasmid mutagenesis protocol. *BMC Biotechnol.* **8**, 91 (2008).
55. Batty, T. G., Kontogiannis, L., Johnson, O., Powell, H. R. & Leslie, A. G. iMOSFLM: a new graphical interface for diffraction-image processing with MOSFLM. *Acta Crystallogr. D. Biol. Crystallogr.* **67**, 271–281 (2011).
56. Winter, G. xia2: an expert system for macromolecular crystallography data reduction. *J. Appl. Crystallogr.* **43**, 186–190 (2010).
57. Winter, G. et al. DIALS: implementation and evaluation of a new integration package. *Acta Crystallogr. D. Biol. Crystallogr.* **74**, 85–97 (2018).
58. Emsley, P. & Cowtan, K. Coot: model-building tools for molecular graphics. *Acta Crystallogr. D. Biol. Crystallogr.* **60**, 2126–2132 (2004).
59. Murshudov, G. N., Vagin, A. A. & Dodson, E. J. Refinement of macromolecular structures by the maximum-likelihood method. *Acta Crystallogr. D. Biol. Crystallogr.* **53**, 240–255 (1997).
60. Sali, A. & Blundell, T. L. Comparative protein modelling by satisfaction of spatial restraints. *J. Mol. Biol.* **234**, 779–815 (1993).
61. Søndergaard, C. R., Olsson, M. H. M., Rostkowski, M. & Jensen, J. H. Improved treatment of ligands and coupling effects in empirical calculation and rationalization of pKa values. *J. Chem. Theory Comput.* **7**, 2284–2295 (2011).
62. Shapovalov, M. V. & Dunbrack, R. L. Jr. A smoothed backbone-dependent rotamer library for proteins derived from adaptive kernel density estimates and regressions. *Structure* **19**, 844–858 (2011).
63. Frisch, M. J. et al. *Gaussian 16 Rev. A.03*. (Gaussian, Inc., Wallingford, CT, 2016).
64. Wang, J., Wang, W., Kollman, P. A. & Case, D. A. Automatic atom type and bond type perception in molecular mechanical calculations. *J. Mol. Graph. Model.* **25**, 247–260 (2006).
65. Maier, J. A. et al. ff14SB: Improving the accuracy of protein side chain and backbone parameters from ff99sb. *J. Chem. Theory Comput.* **11**, 3696–3713 (2015).
66. Steinbrecher, T., Latzer, J. & Case, D. A. Revised AMBER Parameters for bioorganic phosphates. *J. Chem. Theory Comput.* **8**, 4405–4412 (2012).
67. Meagher, K. L., Redman, L. T. & Carlson, H. A. Development of polyphosphate parameters for use with the AMBER force field. *J. Comput. Chem.* **24**, 1016–1025 (2003).
68. Duarte, F. et al. Force field independent metal parameters using a nonbonded dummy model. *J. Phys. Chem. B.* **118**, 4351–4362 (2014).
69. Liao, Q., Pabis, A., Strodel, B. & Kamerlin, S. C. L. Extending the nonbonded cationic dummy model to account for ion-induced dipole interactions. *J. Phys. Chem. Lett.* **8**, 5408–5414 (2017).
70. Case, D. A. et al. Amber 2016. University of California, San Francisco, CA, 2016.
71. Jorgensen, W. L., Chandrasekhar, J., Madura, J. D., Impey, R. W. & Klein, M. L. Comparison of simple potential functions for simulating liquid water. *J. Chem. Phys.* **79**, 926–935 (1983).
72. Berendsen, H. J. C., Postma, J. P. M., van Gunsteren, W. F., DiNola, A. & Haak, J. R. Molecular dynamics with coupling to an external bath. *J. Chem. Phys.* **81**, 3684–3690 (1984).
73. Ryckaert, J.-P., Ciccotti, G. & Berendsen, H. J. C. Numerical integration of the cartesian equations of motion of a system with constraints: molecular dynamics of n-alkanes. *J. Comput. Phys.* **23**, 327–341 (1977).
74. Schneider, T. & Stoll, E. Molecular-dynamics study of a three-dimensional one-component model for distortive phase transitions. *Phys. Rev. B.* **17**, 1302–1322 (1978).
75. Darden, T., York, D. & Pedersen, L. Particle mesh Ewald: An N-log(N) method for Ewald sums in large systems. *J. Chem. Phys.* **98**, 10089–10092 (1993).
76. Roe, D. R. & Cheatham, T. E. PTRAJ and CPPTRAJ: Software for Processing and Analysis of Molecular Dynamics Trajectory Data. *J. Chem. Theory Comput.* **9**, 3084–3095 (2013).
77. Grant, B. J., Rodrigues, A. P. C., ElSawy, K. M., McCammon, J. A. & Caves, L. S. D. Bio3d: an R package for the comparative analysis of protein structures. *Bioinformatics* **22**, 2695–2696 (2006).

Acknowledgements

This work was supported by the Biotechnology and Biological Sciences Research Council (BBSRC) [Grant BB/M010996/1] via EASTBIO Doctoral Training Partnership studentships to B. J. R. and G. F., by Stiftelsen Olle Engkvist Byggmästare [Grant 190-0335] and the Knut and Alice Wallenberg Foundation [Grants 2018.0140 and 2019.0431] to S.C.L.K., and by the European Union’s Horizon 2020 Research and Innovation Programme via a Marie Skłodowska-Curie fellowship [Grant 890562] to M.C. The simulations were enabled by resources provided by the Swedish National Infrastructure for Supercomputing (SNIC, UPPMAX), partially funded by the Swedish Research Council [Grant 2016-07213]. X-ray diffraction data from R56A-*PaATPPRT* crystals were collected at Diamond Light Source in the UK. The authors thank Dr Huanting Liu of the University of St Andrews for advice on site-directed mutagenesis.

Author contributions

G.F. carried out all experimental work except where noted, and wrote the manuscript. B.J.R. expressed and purified *AbHisZ* and carried out the sequence comparison with *PaHisZ*. J.N. expressed and purified R32/R56A/K57A-*PaHisG_S*. M.S.A. supervised the protein crystallography work. M.C. carried out the computational chemistry work and wrote the manuscript. S.C.L.K. supervised the computational chemistry work and wrote the manuscript. R.G.d.S. conceived and supervised the research and wrote the manuscript. All authors analysed data.

Competing interests

The authors declare no competing interests.

Additional information

Supplementary information The online version contains supplementary material available at <https://doi.org/10.1038/s41467-022-34960-9>.

Correspondence and requests for materials should be addressed to Shina C. L. Kamerlin or Rafael G. da Silva.

Peer review information *Nature Communications* thanks Andrew Murkin and the other, anonymous, reviewer(s) for their contribution to the peer review of this work. Peer reviewer reports are available.

Reprints and permissions information is available at <http://www.nature.com/reprints>

Publisher’s note Springer Nature remains neutral with regard to jurisdictional claims in published maps and institutional affiliations.

Open Access This article is licensed under a Creative Commons Attribution 4.0 International License, which permits use, sharing, adaptation, distribution and reproduction in any medium or format, as long as you give appropriate credit to the original author(s) and the source, provide a link to the Creative Commons license, and indicate if changes were made. The images or other third party material in this article are included in the article's Creative Commons license, unless indicated otherwise in a credit line to the material. If material is not included in the article's Creative Commons license and your intended use is not permitted by statutory regulation or exceeds the permitted use, you will need to obtain permission directly from the copyright holder. To view a copy of this license, visit <http://creativecommons.org/licenses/by/4.0/>.

© The Author(s) 2022